Ultrafast magneto-optics in ferromagnetic III–V semiconductors

2006 J. Phys.: Condens. Matter 18 R501

(http://iopscience.iop.org/0953-8984/18/31/R01)

INSTITUTE OF PHYSICS PUBLISHING JOURNAL OF PHYSICS: CONDENSED MATTER

J. Phys.: Condens. Matter **18** (2006) R501–R530 doi:10.1088/0953-8984/18/31/R01

TOPICAL REVIEW

Ultrafast magneto-optics in ferromagnetic III–V semiconductors

Jigang Wang[1,6], Chanjuan Sun[1], Yusuke Hashimoto[1,7], Junichiro Kono[1,8], Giti A Khodaparast[2], Łukasz Cywiński[3], L J Sham[3], Gary D Sanders[4], Christopher J Stanton[4] and Hiro Munekata[5]

[1] Department of Electrical and Computer Engineering, Rice University, Houston, TX 77005, USA
[2] Department of Physics, Virginia Tech., Blacksburg, VA 24061, USA
[3] Department of Physics, University of California at San Diego, San Diego, CA 92093, USA
[4] Department of Physics, University of Florida, Gainesville, FL 32611, USA
[5] Imaging Science and Engineering Laboratory, Tokyo Institute of Technology, Yokohama, Kanagawa 226-8503, Japan

E-mail: kono@rice.edu, khoda@vt.edu, lsham@ucsd.edu, stanton@phys.ufl.edu and hiro@isl.titech.ac.jp

Received 19 April 2006, in final form 4 July 2006
Published 21 July 2006
Online at stacks.iop.org/JPhysCM/18/R501

Abstract

We investigate various ultrafast optical processes in ferromagnetic (III,Mn)V semiconductors induced by femtosecond laser pulses. Two-colour time-resolved magneto-optical spectroscopy has been developed, which allows us to observe a rich array of dynamical phenomena. We isolate several distinct temporal regimes in spin dynamics, interpreting the fast (<1 ps) dynamics as spin heating through sp–d exchange interaction between photo-carriers and Mn ions while the ∼100 ps component is interpreted as a manifestation of spin–lattice relaxation. Charge carrier and phonon dynamics were also carefully studied, showing an ultrashort charge lifetime of photo-injected electrons (∼2 ps) and propagating coherent acoustic phonon wavepackets with a strongly probe energy dependent oscillation period, amplitude and damping.

(Some figures in this article are in colour only in the electronic version)

Contents

[6] Present address: Lawrence Berkeley National Laboratory, Berkeley, CA 94720, USA.
[7] Present address: Imaging Science and Engineering Laboratory, Tokyo Institute of Technology, Yokohama, Kanagawa 226-8503, Japan.
[8] Author to whom any correspondence should be addressed.

1. Introduction

1.1. Motivation: spin-related phenomena and devices

Over the past several years there has been considerable interest and progress in exploring and understanding spin states and dynamics in semiconductor systems including magnetic semiconductors. Using electron spin in addition to the charge can lead to devices with new or improved functionality. Even prior to the discovery of giant magnetoresistance (GMR) [1] where the resistance of thin films of ferromagnetic/nonmagnetic structures is strongly magnetic field dependent, magnetism in metals has been the main basis of information storage. The GMR effect is now used in computer hard drives as well as devices such as magnetometers and nonvolatile memory chips [2]. The GMR effect is considered an early example of the new field of spintronics.

One practical method of developing spin-based devices or spintronics would be to incorporate ferromagnetism in a semiconductor by introducing magnetic dopants such as Mn. The first successful doping of Mn ions into InAs exceeding the heavy doping regime was reported by Munekata and co-workers in 1989 [3]. The subsequent discovery of ferromagnetism in p-type InMnAs films in 1991 triggered great interest in this sample system [4]. Furthermore, Curie temperatures as high as 35 K were obtained as early as 1993 by using InMnAs/(Al, Ga)Sb heterostructures instead of films [5]. This system serves as a prototype for incorporating spin into semiconductors. Subsequently, the growth of ferromagnetic GaMnAs and InGaMnAs was reported in 1996 and 2002, respectively [6, 7]. In addition, several other relevant materials, such as GaMnN, AlCrN, and ZnCoO, have exhibited ferromagnetism [2]. Ferromagnetic semiconductors with Curie temperatures T_c above room temperature can lead to devices such as light emitting diodes and lasers with polarized emission, integrated logic, and memory [2]. Several successful attempts have been reported recently to push the ferromagnetic transition temperatures above 300 K. For instance, room-temperature ferromagnetic order in TiO_2:Co has been observed and T_c in CrAs and CrSb with zinc blende structure is over 400 K [8–10]. In addition, T_c in Mn-delta-doped, Be-modulation-doped GaMnAs heterostructures has reached 250 K, approaching room temperature [11].

These developments are an indication that exploring and understanding spin-dependent phenomena in magnetic semiconductors may one day lead to useful and innovative devices. One important aspect of ferromagnetism in (III,Mn)V semiconductors is its carrier-mediated

nature. Namely, the ferromagnetic exchange interaction between Mn ions is mediated by carriers, and thus, magnetic properties can be changed by changing the carrier density. Koshihara *et al* demonstrated that ferromagnetism can be photo-induced in InMnAs/GaSb heterostructures when sufficient carries are created at temperatures near T_c [12]. In addition, electrical tuning of ferromagnetic order has been demonstrated in InMnAs-based field effect devices [13].

The scope of this review article is to demonstrate the strength of magneto-optical spectroscopy when it is combined with femtosecond laser pulses. Time-resolved magneto-optical spectroscopy can provide direct time-domain information about magnetic properties of excited states with high temporal resolution and fine control. In particular, it has provided essential contributions to our understanding of spin relaxation, spin coherent effects and dephasing phenomena in semiconductors and their quantum-confined structures, a critical stimulus for the field of semiconductor spintronics [14]. Newly developed two-colour methods of magneto-optical Kerr effect (MOKE) and magnetic circular dichroism (MCD) spectroscopy, which are shown to be appropriate for investigating (1) spin relaxation of nonequilibrium photo-excited carriers, (2) transient modifications of ferromagnetic order, and (3) photo-induced dynamic phase transitions, will be discussed. Results for several (III,Mn)V semiconductors including InMnAs, InGaMnAs, and GaMnAs will be described.

1.2. Ultrafast dynamics of magnetically ordered materials

There is much current interest in dynamical processes in *magnetically ordered* systems, both from scientific and technological viewpoints [15]. Pumping a magnetic system with ultrashort laser pulses can strongly alter the thermodynamic equilibrium among the constituents (carriers, spins, and the lattice), triggering a variety of dynamical processes. Investigating these processes can provide estimates for the timescales and strengths of various microscopic interactions and shed new light on how to alter an ordered phase of many-body spin systems through these interactions on very fast timescales. In addition, fascinating phenomena such as ultrafast photo-induced and photo-controlled dynamic phase transitions can be studied.

Both metallic and insulating magnets have been studied extensively using various time-resolved magneto-optical techniques. In particular, the discovery of *ultrafast demagnetization* [16] suggested an ultrafast scheme for magneto-optical data writing. In extreme cases, intense laser pulses were shown to drive a ferromagnetic to paramagnetic phase transition on a femtosecond timescale [17]. Despite the large number of studies performed to date, exactly how a laser pulse can effectively change the magnetic moment and the microscopic effective energy transfer channels among the subsystems are still not understood [18–20]. This is partially due to the fact that, in the case of metallic ferromagnets, the distinction between the 'carriers' and 'spins' is subtle, as the itinerant electrons contribute to both transport and magnetism. In turn direct microscopic coupling between the electronic orbital degree of freedom and the collective spins, leading to extremely fast demagnetization on a femtosecond timescale, is not well understood. On the other hand, antiferromagnetic insulators have shown much slower dynamics, typically of the order of hundreds of picoseconds [21], although femtosecond demagnetization has been predicted [22], and ultrafast control of magnetism using off-resonance excitation has been shown experimentally [23].

Carrier-induced ferromagnetism in (III,Mn)V semiconductors provides an interesting alternative for studying ultrafast magnetization dynamics. Unlike in ferromagnetic metals, there is a clear distinction between mobile carriers (holes) and localized spins (Mn ions) and ferromagnetic order is realized through their strong coupling (p–d exchange interaction). This coupling in turn makes the magnetic order sensitive to carrier density changes via external perturbations, e.g., electrical gating fields or optical radiation [12, 13, 24]. In addition, since

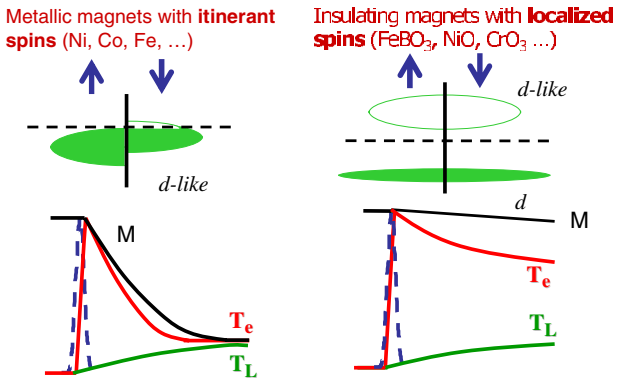

Figure 1. An overview of band diagrams as well as the demagnetization dynamics in metallic and insulating magnets, respectively.

two separate issues of current interest, i.e., hole relaxations and collective magnetization dynamics, fall into one platform, their correlation, which is rarely addressed elsewhere, could be investigated.

2. Prior ultrafast optical studies of magnetically ordered systems

2.1. Metallic and insulating magnets

In this section, we will briefly review some of the main ultrafast magneto-optical studies performed on metallic and insulating ferromagnets. Figure 1 shows simplified physical scenarios for the magnetic dynamics of metallic (left) and insulating (right) systems. Here, the established knowledge about different dynamic processes induced by femtosecond laser excitations in these two systems is summarized. In itinerant ferromagnets, the pump-induced magnetization change mostly follows the thermalization of the hot electron population with a characteristic timescale of 100 fs (left panel, figure 1). On the other hand, in insulating magnets, a much slower demagnetization process is observed with a characteristic timescale of hundreds of picoseconds (right panel, figure 1).

Ultrafast demagnetization in a metallic magnet was first reported by Bigot's group in 1996 [16]. Using time-resolved MOKE to study 22 nm thick Ni films, the authors observed an ultrafast reduction in MOKE angle, of the order of a few picoseconds, which was interpreted as induced demagnetization (left panel, figure 2 [16]). In extreme cases, intense laser pulses were shown to increase the electron temperature even above the Curie temperature, driving a ferromagnetic to paramagnetic phase transition on a femtosecond timescale; it occurred within 500 fs, before heating of the lattice. The right panel of figure 2 shows an example of complete quenching of ferromagnetism induced by a laser pulse, of the order of 100 fs in $CoPt_3$ [16, 17].

Exactly how a laser pulse can effectively change the collective magnetization in an ultrafast manner is still an open question; the interpretation of the observed transient magneto-optical signal in terms of magnetization dynamics, especially in the femtosecond timescale, remains controversial, motivating further experimental investigations. Different ultrafast magneto-optical techniques, such as magnetic surface second-harmonic generation (SHG) and spin-resolved photo-emission, have been used by different groups and similar sub-picosecond dynamics has been observed. However, there are still discrepancies in the details of the experimental data obtained by different groups, which lead to various interpretations of spin dynamics. Finally, it should be mentioned that, in the case of high pump fluences where a complete quenching of the magnetic order occurs, the interpretation is unambiguous since

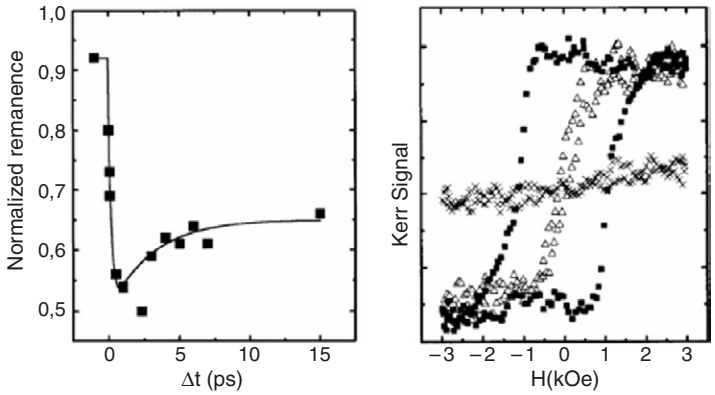

Figure 2. Femtosecond demagnetization in ferromagnetic metals Ni and $CoPt_3$, respectively. Left panel: the normalized remnant magnetization for a Ni film decreased within the first 1 ps after photo-excitation. Right panel: in $CoPt_3$, the ferromagnetic hysteresis loops at different time delays show that a ferromagnet was converted to its paramagnetic state after ∼500 fs [16, 17].

the material switches to its opposite magnetic state when it is kept in a static magnetic field with an amplitude slightly less than the coercive field (right panel, figure 2). Therefore, in ferromagnetic metals, this convincing argument together with the experimental evidence from both time-resolved magnetic SHG and MOKE measurements indicates that the intrinsic magnetization can indeed be switched on a femtosecond timescale.

Very different demagnetization dynamics has been reported for insulating magnets, as compared to their metallic counterpart (figure 1), due to several fundamental differences in magnetic states and transport properties between the two types of magnets. Generally speaking, virtual hopping among localized spin sates in magnetic insulators leads to an antiferromagnetic superexchange interaction, while interacting itinerant spins in magnetic metals favour a ferromagnetic exchange splitting of spin up and spin down energy bands. Because of the localized character of the magnetic moments and absence of intrinsic doping carriers in insulating magnets, the primary effect of a femtosecond pump pulse is lattice heating, which is followed by heating of the collective spin system via magnon generation.

Such a picture is supported by the recent observations in $FeBO_3$ [21]. Weak ferromagnetic order, coexisting with largely antiferromagnetically coupled spins, was probed via the Faraday effect, indicating ∼500 ps magnetization quenching dynamics. It is also interesting to note that several recent theoretical many-body calculations in insulating magnets, e.g., nickel oxide, also predict demagnetization times shorter than 100 fs [22], which still need further experimental confirmation. Recently, femtosecond magnetization dynamics has indeed been shown experimentally for antiferromagnetic (AFM) materials, demonstrating ultrafast reorientation and precession of the AFM order parameters using either on- or off-resonance excitation [23, 25]. These observations, taking advantage of some unique properties of AFM systems, i.e., lack of macroscopic magnetization and exchange field enhanced magnetic resonance frequency, have stimulated new interest in these materials.

2.2. (III,Mn)V semiconducting ferromagnets

In this section, prior work concerning the ultrafast dynamics of ferromagnetic (III,Mn)V is reviewed. One of the first reports on spin dynamics in ferromagnetic GaMnAs was from Gonokami's group [26] where the measurements were performed on a sample of 1.05 μm

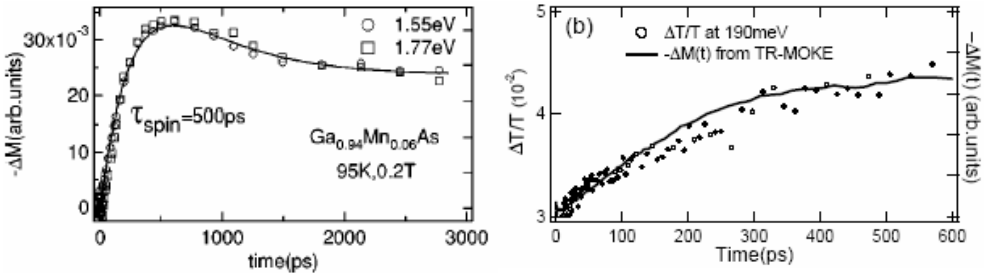

Figure 3. Demagnetization dynamics in GaMnAs reported by Kojima *et al* [26, 27]. Left: time-dependent magnetization measured through time-resolved MOKE. The rise of the signal, of the order of several hundreds of picoseconds, indicates a relatively slow demagnetization dynamics, compared to the metallic case. Right: extracted spin-related slow component in differential transmission (left axis) compared with time-dependent magnetization obtained by time-resolved MOKE (right axis) [27].

thick GaMnAs film grown by MBE on a GaAs[001] substrate. A two-colour probe method of time-resolved MOKE was used to study time-dependent magnetization (left, figure 3). A photo-induced demagnetization process was clearly observed but the magnetization drop occurred of the order of 1 ns, similar to that of the pulse laser excited insulating magnets, although the free carrier lifetime of the photo-generated electrons was within 1 ps, as measured in a separate experiment. This type of demagnetization dynamics is further supported by a later differential transmission experiment from the same group, using mid-infrared probe pulses to couple with the transition related to Mn impurities [27]. The experimental data exhibited a strongly temperature-dependent slow component, denoted as $\Delta T/T_{\mathrm{mag}}$ (right, figure 3), which coincides with time-dependent magnetization revealed by time-resolved MOKE.

Kojima *et al* [27] claimed that the observed, very different temporal behaviours of charge carrier and demagnetization dynamics, called the spin-charge thermal isolation, originated from the high degree of spin polarization near the Fermi level. They also inferred that the half-metallic nature of electronic bands in GaMnAs gave rise to the observed phenomena and the carriers responsible for mediating ferromagnetic exchange coupling were mostly d-like.

While most of the prior experiments on either metallic or insulating magnets concentrated on demagnetization dynamics, work by Munekata's group showed photo-induced magnetization rotation in GaMnAs via optically injected spin polarized carriers [28]. The basic ideas for photo-induced Mn spin rotation (and even photo-induced ferromagnetic order) have been a research focus since the 1980s, largely in paramagnetic semiconductors. For instance, photo-induced Mn spin precession was reported by Crooker *et al* in (II,Mn)VI-based quantum well structures [29]. The current renewed interest in (III,Mn)V semiconductors originates from the fact that the magnetic order in III–V ferromagnetic semiconductors is carrier mediated and there is a very strong mutual interaction between the two spin ensembles, carriers and Mn sublattice, via p–d exchange coupling. Photo-induced magnetization rotation in a ferromagnetic semiconductor was first demonstrated in a CW type experiment by Oiwa *et al* (left, figure 4) [24]. Here, a thin (Ga, Mn)As epilayer (∼200 nm) on top of a GaAs buffer layer results in in-plane magnetic anisotropy, exhibiting no noticeable remanent component along the direction normal to the sample at zero magnetic field, as seen in the inset of the left panel of figure 4. There are clearly out-of-plane magnetization components with CW light irradiation, exhibiting a strong dependence on the polarization state of the light. To gain more insight into such photo-induced magnetization rotation from in-plane to out-of-plane and differentiate

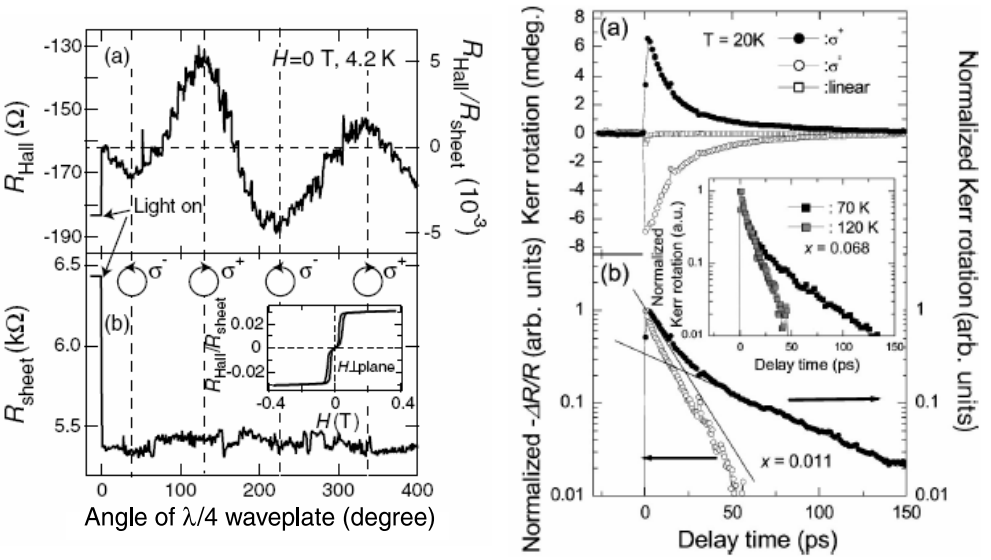

Figure 4. Left: changes in Hall resistance and sheet resistance at 4.2 K for a GaMnAs/GaAs sample under CW light irradiation, whose polarization state is controlled by a quarter-waveplate. The inset shows the magnetization curve extracted from the anomalous Hall effect measurements, indicating in-plane magnetic anisotropy of the current sample. Right: time-resolved MOKE and reflectivity at 20 K, below the transition temperature, for two different samples excited by three different polarization conditions. Adapted from [24, 28].

it from effects from polarized carrier spins, time-resolved MOKE was used to directly obtain time-domain information (right, figure 4) [28]. Indeed, the enhanced MOKE signal amplitude and a second decay component accompanying the photo-excited carrier spin relaxation process were observed only below T_c. The different power and temperature dependence of the two decay components further corroborate the authors' claim of photo-induced magnetization rotation.

Kimel *et al* have also performed time-resolved MOKE to study magnetization dynamics after femtosecond excitation in GaMnAs [21]. In their measurements, the authors could not reproduce any of these observations. There is neither an indication for ultrafast demagnetization nor evidence for precessional motion of Mn spins. The time-resolved magneto-optical signal was completely independent of temperature, indicating that it was probably from optically injected carrier spins instead of collective spins. Therefore, Kimel *et al* concluded that there is no significant coupling between photo-injected carriers and Mn collective spins.

As reported above, experimental results obtained by different groups for GaMnAs led to very different interpretations of spin dynamics. In this context, two main issues should be kept in mind: in which excitation regime was the particular experiment performed and how much does spin dynamics depend on the particular sample? For instance, the maximum peak fluences used in the demagnetization and photo-induced rotation measurement were of the order of 1 mJ cm^{-2} per pulse and 1 μJ cm^{-2} per pulse, respectively. In the work of Kimel and co-workers [21], although the same type of laser and similar experimental conditions as the photo-induced magnetization rotation measurements were used, very different observations led to conflicting conclusions. These may come from the details of sample preparation. The (III,Mn)Vs, being prepared using low-temperature MBE, are highly disordered systems and magnetic properties of samples critically depend on multiple parameters, i.e., film thickness, growth temperature, and post-growth annealing. All these complications may lead to different

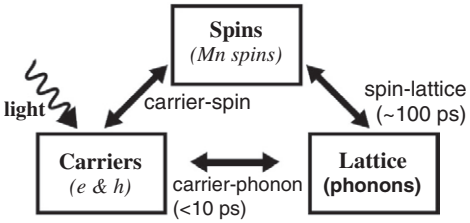

Figure 5. Three reservoirs (carriers, spins, lattice) taking part in the light-induced demagnetization process. The descriptions in italics are specific to the (III,Mn)V case. Out of the three possible interaction channels, spin–lattice and carrier–phonon are quite well understood. The direct carrier–spin coupling is a subject of current research. In (III,Mn)V ferromagnetic semiconductors the carrier-spin mechanism is the sp–d interaction between the spins of delocalized carriers and the localized Mn spins.

experimental observations, even under the same experimental conditions. Better control, understanding and characterizations of (III,Mn)V growth processes are needed to further reconcile various experimental observations.

2.3. Theoretical models

Most of the theoretical work on magnetization dynamics driven by photo-excitation in diluted magnetic semiconductors has been concerned with the coherent regime, where the polarization and/or the phase of light are important [30–33]. A proposal for exciting below the band gap to coherently induce ferromagnetism in a paramagnetic (II,Mn)VI compound has also been put forth [34]. In the following we will review the theoretical approaches to ultrafast demagnetization, which is an incoherent process involving heating of the spin subsystem. Investigations of this phenomenon have been concentrated on metals, but the main ideas described below also apply to the semiconductor case. Our model of quenching of ferromagnetic order in (III,Mn)V ferromagnetic semiconductors is described in more detail in section 4.3.4.

There are three reservoirs involved in the light-induced demagnetization process, which we denote as carriers, spins and lattice (see figure 5). Energy and angular momentum can be exchanged between them: the mechanisms and timescales for the carrier–lattice and spin–lattice couplings are quite well understood (especially the former). In the standard process of laser-induced demagnetization, as used in magneto-optical recording [35], the light pulse excites carriers, which then equilibrate with the lattice on a timescale of picoseconds. The heat deposited in the lattice is then transferred into the spin system through the spin–lattice interaction. The heating up of the spins then results in demagnetization, occurring on the timescale of the spin–lattice relaxation time τ_{sl}, which is at least of the order of 100 ps. Experiments show $\tau_{sl} \approx 80$ ps in Gd [36], between 30 ps and 20 ns in Fe [37] and more than nanoseconds in paramagnetic CdMnTe [38]. In order to explain the ultrafast demagnetization, the existence of the direct coupling between the carrier and spin reservoir has to be invoked. The microscopic mechanism of this coupling is a key theoretical problem in this field.

The distinction between the first two reservoirs (carriers and spins) is only clear in materials whose magnetic properties are dominated by localized spins, such as rare-earth ferromagnets and ferromagnetic semiconductors (see section 4.3.4). In the case of itinerant ferromagnets, in which most of the ultrafast demagnetization studies have been performed, the distinction between the 'carriers' and the 'spins' is subtle, as itinerant electrons contribute both to transport and magnetism. This is a serious impediment in the creation of a simple

theory of ultrafast demagnetization in metals. In ferromagnetic semiconductors, there is a sharp separation between the mobile carriers (holes) and localized spins (Mn ions), which makes such a distinction between carrier and spin populations more natural.

The physical mechanism through which the orbital (carrier) degree of freedom can couple to the spin degree of freedom is the spin–orbit interaction. It underpins the process of spin–lattice relaxation, in which the spins are scattered by fluctuations of the crystal fields produced by phonons [39]. In order to explain the ultrafast demagnetization, one has to formulate the theory of direct coupling of charge and spin degrees of freedom, which includes the spin–orbit interaction.

In a seminal paper [16] on demagnetization in nickel, a phenomenological three-temperature model was used to fit the experimental data. This is an extension of a model describing the thermal relaxation of electrons in metals (see e.g. [40]). In [16] the three reservoirs were described by respective temperatures, and the demagnetization resulted from the changes in spin temperature. The equations of the heat flow were of the simple form

$$C_{\mathrm{e}}(T_{\mathrm{e}})\frac{\mathrm{d}T_{\mathrm{e}}}{\mathrm{d}t} = -G_{\mathrm{el}}(T_{\mathrm{e}} - T_{\mathrm{l}}) - G_{\mathrm{es}}(T_{\mathrm{e}} - T_{\mathrm{s}}) + P(t) \tag{1}$$

$$C_{\mathrm{s}}(T_{\mathrm{s}})\frac{\mathrm{d}T_{\mathrm{s}}}{\mathrm{d}t} = -G_{\mathrm{es}}(T_{\mathrm{s}} - T_{\mathrm{e}}) - G_{\mathrm{sl}}(T_{\mathrm{s}} - T_{\mathrm{l}}) \tag{2}$$

$$C_{\mathrm{l}}(T_{\mathrm{l}})\frac{\mathrm{d}T_{\mathrm{l}}}{\mathrm{d}t} = -G_{\mathrm{el}}(T_{\mathrm{l}} - T_{\mathrm{e}}) - G_{\mathrm{sl}}(T_{\mathrm{l}} - T_{\mathrm{s}}) \tag{3}$$

where e, s, l denote the electronic, spin and lattice reservoirs, with corresponding specific heat coefficients C_{a} and coupling constants G_{ab}. It should be stressed that although the value of the direct carrier–spin interaction constant G_{es} could be fitted to experimental data, this phenomenological model does not say anything about the microscopic coupling mechanism. The other serious shortcoming of this approach is the description solely in terms of the heat flow, neglecting the fact that the angular momentum also has to be exchanged between the reservoirs. Recently, simplified but transparent theories involving the processes of angular momentum transfer have been proposed independently for metals such as Ni [41, 42] and ferromagnetic semiconductors such as InMnAs [43]. In both cases, the Eliot–Yafet spin relaxation of carriers [44] transfers the angular momentum into the lattice, which is treated as a perfect sink. In [41, 42] somewhat artificial, but conceptually convenient, separation of carrier and spin systems in a ferromagnetic metal is assumed. In our work [43] we use a well-established model of the carrier–spin coupling in ferromagnetic semiconductors [45], and fast spin relaxation of holes turns out to be crucial for the explanation of experimental results. The detailed account of this model is given in section 4.3.4.

Another theoretical work is that of Zhang and Hübner [20], who have calculated laser-induced dynamics within a simplified many-body model of a ferromagnet. They obtained complete quenching of magnetization within the pulse time, and they ascribed it to a cooperative effect of spin–orbit coupling and the laser field. But even though the early experiments suggested demagnetization occurred within the pulse width, corrections to the Kerr signal interpretation due to dichroic bleaching [18] (see below) have led to an estimate of the demagnetization timescale of a couple of hundreds of femtoseconds. Consequently, even if the light-assisted mechanism is relevant, it is not the whole story in the sub-picosecond regime.

We should also mention the calculations of time-resolved magneto-optical response of highly excited ferromagnets [46, 47]. Although they do not calculate the real demagnetization, they address the problem of the influence of the dichroic bleaching on the observed Kerr signal and show that this phenomenon is very important for the proper interpretation of the observed magneto-optical signal. It has been first noted in [18] that in the regime of high excitation the measured magneto-optical signal S (e.g., Kerr rotation, ellipticity, Faraday rotation, etc)

need not be proportional to the instantaneous magnetization. In the steady state we can write $S = f(\hbar\omega)M$, where f depends on the diagonal elements of the dielectric tensor and M is the magnetization, but after the excitation we obtain $\Delta S = M\Delta f + f\Delta M$ where only the second component represents the real magnetization dynamics. The theoretical calculations clearly show the visible influence of the $M\Delta f$ factor on the magneto-optical signal on ultra short timescales. In experiments, much effort has been put into the extraction of the purely 'magnetic' contribution, by methods such as measuring more than one magneto-optical quantity at the same time [18, 26, 48] or by forming a linear combinations of the same quantity measured in different conditions (e.g., for different temperatures) [49, 50]. In our investigations, we have used a two-colour setup (section 3.2) where the use of different wavelengths for the two pulses of light minimizes the effects of pump-induced state filling felt by the probe.

3. Ultrafast magneto-optical techniques

3.1. Commonly used ultrafast spin-resolved techniques

In order to study ultrafast magnetization dynamics, it is important to develop magneto-optical spectroscopy techniques with decent signal-to-noise ratio and high temporal resolution. To achieve these goals several types of experimental detection scheme have been developed, including time-resolved linear magneto-optical effects (Kerr effects in reflection or Faraday effect in transmission geometry), spin-resolved photo-emission, and time-resolved magnetic second-harmonic generation (MSHG) techniques [15, 51–53]. In these experiments, a pump–probe configuration, combined with femtosecond laser pulses, is used to obtain temporal resolution and a static magnetic field could be used to control the initial magnetic state of the sample. Next we concentrate on two linear magneto-optical effects, namely MOKE and reflection magnetic circular dichroism (MCD), and discuss how to implement these in our time-resolved measurements. In addition, in section 3.3 we briefly discuss MSHG techniques.

3.2. Two-colour MOKE techniques

We have developed a two-colour MOKE/MCD spectroscopy setup, which consists of an optical parametric amplifier (OPA) pumped by a Ti:sapphire-based regenerative amplifier (Model CPA-2010, Clark-MXR, Inc.). The OPA is used as a pump tuned around 2 μm and a very small fraction ($\sim 10^{-5}$) [54, 55] of the amplified Ti:sapphire laser beam (775 nm), is used as a probe; the high photon energy of the probe ensures diminished 'dichroic bleaching' effects [18] due to the pump excited carriers.

Figure 6 shows a schematic diagram of the experimental setup. The two-colour MOKE/MCD experiments are carried out in a polar configuration. The pump and probe beams are made parallel and then focused onto the sample mounted inside a magnetic cryostat. A quarter-waveplate is used to control the polarization of the pump and a half-waveplate sets the polarization of the probe. In the case of MOKE measurements, the probe polarization is set to be 45° with respect to the s and p polarization. In the case of MCD, the probe polarization is set to be either horizontal or vertical before hitting the sample and the reflected probe beam passes another quarter-waveplate before detection (figure 6). A Wollaston prism serves as a polarization-dependent beam splitter, which splits the linearly polarized beam into two spatially separated components with polarization directions orthogonal to each other. Two different detection setups are used, i.e., combination of a lock-in amplifier and a differential amplifier (New Focus Nirvana 2007) or two boxcar integrators and two separate identical photo-diodes. We emphasize that the second scheme not only makes it suitable for the detection of short

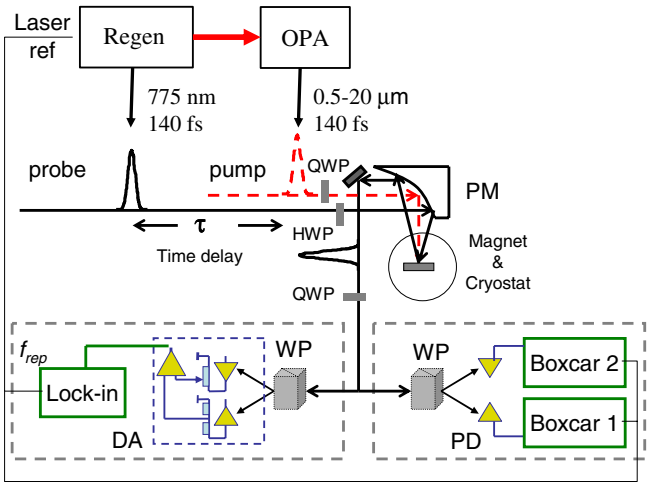

Figure 6. Schematic diagram of two different setups for two-colour, time-resolved MOKE/MCD spectroscopy. Q(H)WP: quarter- (half-) waveplate; PM: gold-coated parabolic mirror; WP: Wollaston prism; DA: differential amplifier; PD: Si photo-diode.

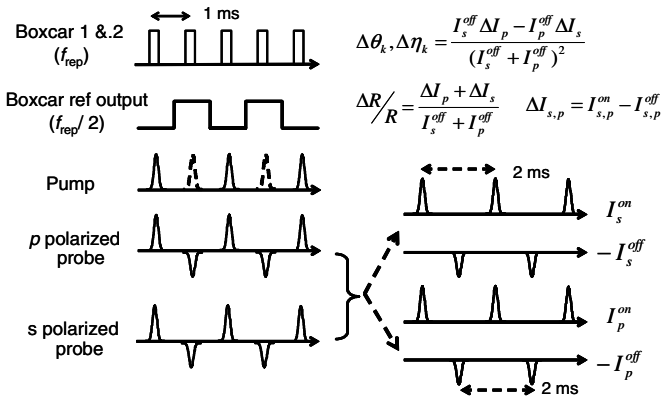

Figure 7. The principle of simultaneously detecting photo-induced MOKE/MCD and differential reflectivity using two boxcar integrators.

low-duty-cycle pulses and greatly reduces the pulse-to-pulse fluctuations from our amplified system, but also has the unique advantage of extracting the polarization and reflectivity changes simultaneously from the same set of raw data, via further computation with some algorithms discussed below.

In order to implement this scheme, the mid-infrared pump is modulated by an optical chopper with a half harmonic of the laser repetition rate (∼500 Hz), i.e., every other pump pulse is blocked. We record the intensity of reflected near-infrared probe pulses, both the s- and p-components, as a function of time delay and magnetic field. Two boxcars, locked to the laser reference and synchronized with each laser shot, are used to simultaneously detect two different polarization states of the probe with and without pump for the adjacent pulses. As shown in figure 7, after recording four sets of raw data at each time delay in one scan, I_s^{on}, I_s^{off}, I_p^{on}, I_p^{off}, which are the s-polarized probe and p-polarized probe with pump and without pump, respectively, we can extract any polarization and reflectivity changes by the following relations. The Kerr rotation angle and ellipticity can be expressed in the following way in the

current experimental condition,

$$\theta_{\mathrm{K}} = \frac{I_{\mathrm{p}} - I_{\mathrm{s}}}{2 \times (I_{\mathrm{p}} + I_{\mathrm{s}})} \tag{4}$$

$$\eta_{\mathrm{k}} = \frac{I_{\mathrm{circular,left}} - I_{\mathrm{circular,right}}}{2 \times (I_{\mathrm{circular,left}} + I_{\mathrm{circular,right}})}. \tag{5}$$

The analytical expression for the photo-induced Kerr rotation is obtained by taking the first derivative of equation (4), i.e.

$$\Delta\theta_{\mathrm{K}} = (I_{\mathrm{s}}^{\mathrm{off}}\Delta I_{\mathrm{p}} - I_{\mathrm{p}}^{\mathrm{off}}\Delta I_{\mathrm{s}})/(I_{\mathrm{s}}^{\mathrm{off}} + I_{\mathrm{p}}^{\mathrm{off}})^2 \tag{6}$$

where $\Delta I_{\mathrm{p}} = I_{\mathrm{p}}^{\mathrm{on}} - I_{\mathrm{p}}^{\mathrm{off}}$ and $\Delta I_{\mathrm{s}} = I_{\mathrm{s}}^{\mathrm{on}} - I_{\mathrm{s}}^{\mathrm{off}}$. We can get an analytical expression for the ellipticity change in a similar way, after replacing I_{s} and I_{p} by $I_{\mathrm{circular,left}}$ and $I_{\mathrm{circular,right}}$, respectively. We can also derive differential reflectivity from the raw data, i.e.

$$\frac{\Delta R}{R} = (\Delta I_{\mathrm{p}} + \Delta I_{\mathrm{s}})/(I_{\mathrm{s}}^{\mathrm{off}} + I_{\mathrm{p}}^{\mathrm{off}}), \tag{7}$$

With the current system, the smallest Kerr angle and differential reflectivity that can be measured is 2×10^{-5} rad and 10^{-4}, using ~5000 pulses.

3.3. Time-resolved MSHG techniques

Time-resolved MSHG has also been applied to study ultrafast magnetization dynamics in several ferromagnetic metals [51, 53]. In general, the nonlinear polarization $P(2\omega)$, responsible for generating second-harmonic field, can be written as

$$P_i(2\omega) = \chi_{ijk}^{(2)} E_j E_k \tag{8}$$

where $\chi_{ijk}^{(2)}$ is the second-order optical susceptibility tensor, which can be decomposed into even (nonmagnetic) and odd (magnetic) components [56]. Time-resolved MSHG techniques allow one to separate these two contributions by carefully measuring second-harmonic intensities as well as their phases for opposite magnetization directions I_+ and I_-, respectively. These can be understood by examining the following analytical expressions for I_+ and I_-,

$$I_+ \propto |\chi_{\mathrm{even}}^{(2)} + \chi_{\mathrm{odd}}^{(2)} \mathrm{e}^{\mathrm{i}\varphi}|^2, \qquad I_- \propto |\chi_{\mathrm{even}}^{(2)} - \chi_{\mathrm{odd}}^{(2)} \mathrm{e}^{\mathrm{i}\varphi}|^2, \tag{9}$$

where φ is the relative phase between even and odd components. More detailed analysis of extracting the phases and reconstructing magnetization induced second-harmonic components can be found in Conrad *et al* [57].

Finally, we want to point out that both two-colour MOKE/MCD and time-resolved MSHG are potentially able to distinguish between ultrafast magnetization components and pure nonlinear optical effects if details of the data are carefully considered.

4. Experimental results and discussion

Next we will discuss charge, phonon and magnetization dynamics in the III–V ferromagnetic semiconductor heterostructures InMnAs/GaSb, GaMnAs/GaAs and InGaMnAs/InGaAs.

4.1. Charge dynamics

4.1.1. Ultrashort charge lifetimes and long-lasting differential reflectivity signals. Typical data showing ultrafast carrier dynamics in ferromagnetic semiconductor InMnAs/GaSb are presented in figure 8(a). Complex carrier decay dynamics is observed. First, the initial change

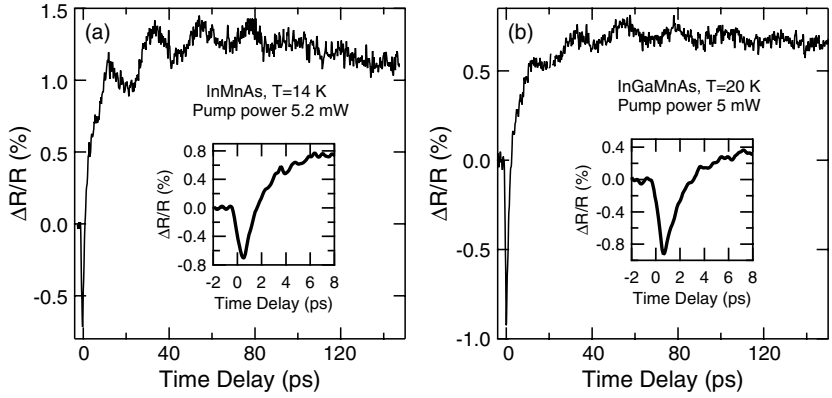

Figure 8. Differential reflectivity of (a) InMnAs and (b) InGaMnAs. Insets: initial decay of ultrafast transients. After photo-excitation, the differential reflectivity shows a sharp negative drop for times less than 2 ps followed by a rapid rise and sign change in the observed differential reflectivity. At longer times (several hundred ps) periodic oscillations in the differential reflectivity are observed with a period of ∼23 ps superimposed on a very slow decay. The pump wavelength was chosen to be 1.2 μm for InGaMnAs and 2 μm in the case of InMnAs, in order to create transient carriers just above the band gap of ferromagnetic semiconductors.

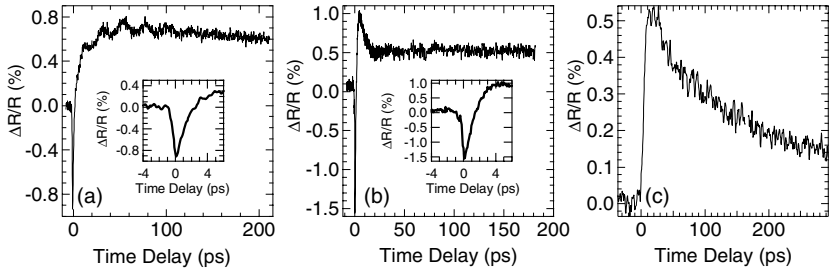

Figure 9. Differential reflectivity of (a) InGaMnAs, (b) LT-InGaAs and (c) HT-InGaAs at 20 K. Experimental conditions are exactly the same for the three cases. Inset (a) and (b): initial decay of ultrafast transients. A similar initial fast reduction and quick sign change is observed in LT-InGaAs, but not in HT-InGaAs.

in the differential reflectivity is negative for times less than 2 ps after photo-excitation (inset of figure 8(a)). Second, a rapid reflectivity rise is observed, leading to a sign change. Next, reflectivity oscillations with a period of ∼23 ps are observed. Finally, the signal shows a very slow decay to zero (several hundred ps).

As seen in figure 8(b), similar complex carrier decay dynamics was also observed in InGaMnAs, which verifies the universality of this type of decay dynamics in ferromagnetic (III,Mn)V systems. In the case of a reference low-temperature grown InGaAs (LT-InGaAs) sample [58] (figure 9(b)), we observed a similar initial negative change in reflectivity and a subsequent fast rise with a sign change. On the other hand, in a high-temperature InGaAs (HT-InGaAs) sample (figure 9(c)), the reflectivity change only showed a single exponential decay with a decay time of ∼104 ps. These facts led us to believe that the fast (∼2 ps) decay of the initial negative signal, observed only in III–V DMSs and LT-InGaAs, reflects a unique feature of low-temperature MBE growth and can be attributed to the ultrafast trapping of electrons (by As_{Ga} antisite defects) and holes (by Ga vacancies), i.e., by mid-bandgap states due to defects. Because of these trapping processes, the free charge carrier life times in III–V ferromagnetic

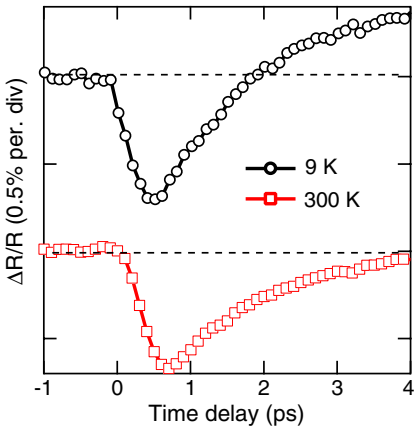

Figure 10. Transient reflectivity of InMnAs at 9 and 300 K.

semiconductors at low temperature are less than 1 ps. Results of the temperature dependence of the ultrafast trapping process are shown in figure 10, which reveals that the trapping time increases with temperature. This behaviour can be qualitatively understood by the argument that thermal fluctuations at the elevated temperature make it harder to trap the photo-generated carriers.

We can qualitatively understand the transient reflectivity response as follows. The initial sharp dip in the differential reflectivity results from free carrier Drude absorption by the hot photo-generated carriers. The photo-generated hot carriers relax back to quasi-equilibrium distributions through the emission of confined LO phonons and the ultrafast trapping of electrons (by As_{Ga} antisite defects) and holes (by Ga vacancies). This alters the dielectric function of the heterostructure through changes in the electron and hole distribution functions and gives rise to the sharp increase and sign change in the differential reflectivity seen in figure 8. The final decay process after the rise in reflectivity suggests slow recombination of the trapped carriers, which finally vacates the carrier traps and causes the differential reflectivity to return to zero. The beginnings of this slow decay in the differential reflectivity can be seen in the long time signal in the differential reflectivity in figure 8.

4.2. Phonon dynamics

4.2.1. Propagating coherent acoustic phonons. In this section, we focus on those periodic oscillations observed in the differential reflectivity. These oscillations are associated with coherent acoustic phonon wavepackets that are generated in the magnetic layer and propagate into the buffer layer.

In the coherent phonon experiment, a 140 fs, mid-infrared pump beam from the OPA and a broadband continuum from 0.6 to 0.95 μm are used to directly detect coherent phonon oscillations in the time domain.

Typical data showing the coherent oscillations of the differential reflectivity in InMnAs/GaSb and InGaMnAs/InGaAs are presented in figure 8. At long times, when the differential reflectivity signal becomes positive, there are periodic oscillations, with a period of ~23 ps for both cases at 775 nm probe wavelength. We applied an external magnetic field of 0, 5, and 9.5 T to the sample and the oscillation period did not change, as shown in figure 11(a). This rules out magnons or quantum beats between Landau levels as a source of the oscillations. Furthermore, our field-dependent experiments show that magnetism does not play a role in the observed oscillations. Next, we varied the pump fluence as shown in figure 11(b). For pump

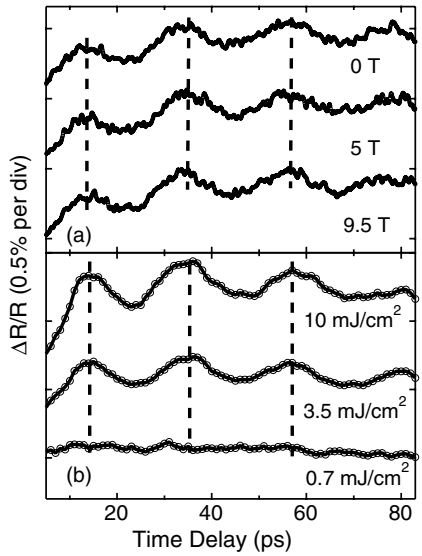

Figure 11. Two-colour pump–probe differential reflectivity oscillations in an InMnAs/GaSb heterostructure. The dependence of the oscillations on magnetic field is shown in (a) while the dependence on pump power is shown in (b). The oscillation period does not change, as shown by the vertical dashed lines [59].

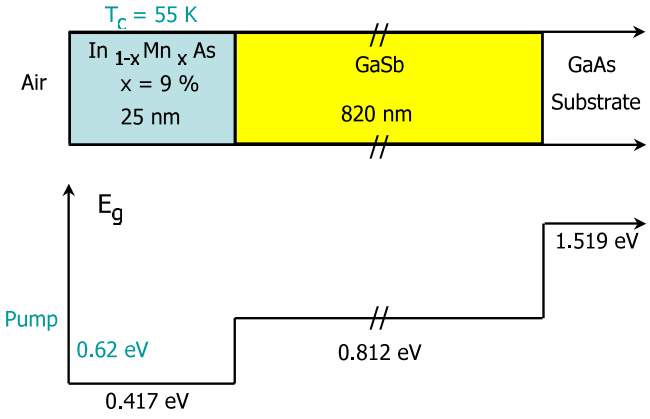

Figure 12. Schematic diagram of the modelled heterostructure consisting of a 25 nm $In_{0.91}Mn_{0.09}As$ quantum well and a 820 nm GaSb barrier grown on a GaAs substrate. The band gap as a function of position in each of the layers is also shown.

fluences of 0.7, 3.5, and 10 mJ cm^{-2}, the intensity of the oscillation changed but the frequency did not. Varying the pump fluence increases the photo-excited carrier density. Since the plasma frequency increases with the total carrier concentration, we would expect the oscillation period to increase with increasing pump fluence if it were related to plasmons. Since the oscillation period is independent of pump fluence, we rule out plasmons as the cause of the oscillations.

Indeed, it has been shown that the oscillations instead resulted from selective photo-excitation in the InMnAs layer which triggered a coherent phonon wavepacket that propagated into the GaSb layer [59]. This was similar to oscillations previously seen in nonmagnetic InGaN/GaN semiconductor heterostructures [60–63].

The main samples studied are shown schematically in figure 12. The InMnAs/GaSb heterostructure consisted of a 25 nm thick magnetic layer with Mn concentration 0.09, grown on a 820 nm thick GaSb buffer layer on a semi-insulating GaAs(001) substrate. Its room-temperature hole density and mobility were 1.1×10^{19} cm^{-3} and 323 cm^2 V^{-1} s^{-1}, respectively,

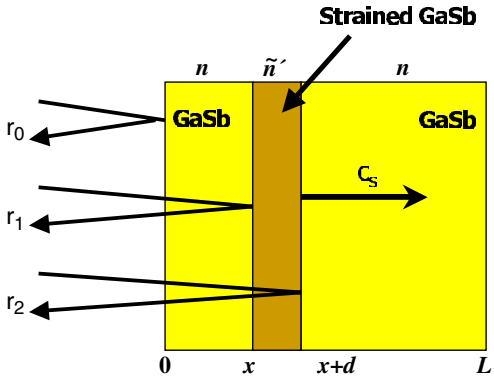

Figure 13. Propagating strained GaSb layer. The pump pulse creates a coherent acoustic phonon wave packet in the InMnAs layer near the surface. The coherent phonon wave packet propagates into the GaSb layer. As the wave packet propagates, there is a small change in the index of refraction of the strained layer compared to the background GaSb. The effects of this change in index can be calculated by assuming a single additional reflection off the front and back surfaces.

estimated from Hall measurements. Detailed growth conditions and sample information can be found in [64, 65].

4.2.2. Simple model. The reflectivity oscillations can be qualitatively understood as follows. The selective absorption of carriers in the InMnAs layer generates a coherent phonon wavepacket which has the thickness of the layer and propagates into the GaSb substrate. This is similar to previous work on InGaN/GaN epilayers where propagating coherent acoustic phonons have been observed [60, 61]. The propagating strain pulse in the GaSb substrate shown in figure 13 gives rise to a perturbation in the GaSb dielectric function and propagates through the layer at the acoustic sound speed. The sample thus acts as a Fabry–Perot interferometer and a simple geometrical optics argument can give us the period for the reflectivity oscillations due to the propagating coherent acoustic phonon wavepacket [60].

In the simplest calculation, one only needs to take into account the (single) additional reflection at the front and rear interfaces of the packet. Multiple reflections can be ignored since the change in reflection is very small (typically one part in 10^{-3}–10^{-6}), and hence the multiple reflections correspond to higher-order terms in $\Delta r/r$.

Assuming that the small change in the index of refraction in the region of the propagating phonon can be written $\tilde{n}' = \tilde{n} + \delta n + \mathrm{i}\Delta\kappa$, where $\tilde{n} = n + \mathrm{i}\kappa$ is the complex background index of GaSb and δn and $\delta\kappa$ are the *changes* to the real and imaginary parts of the refractive index resulting from the propagating coherent acoustic mode. The change in reflectivity is then given by

$$\Delta r = r_1 + r_2 = \mathrm{e}^{\mathrm{i}(2n\omega/c)x}\left(\frac{\tilde{n}' - n}{\tilde{n}' - n}\right)(\mathrm{e}^{\mathrm{i}(2\tilde{n}'\omega/c)d} - 1). \tag{10}$$

If the wavelength of light is large compared to the InMnAs layer thickness, this leads to a change in the reflection coefficient R,

$$\frac{\Delta R}{R} =\sim 2\,\mathrm{e}^{-\alpha x}\frac{\omega}{c}\left(\frac{n+1}{n-1}\right)\mathrm{d}\left[\delta n\sin(2n\omega x/c) + \delta\kappa\cos(2n\omega x/c)\right]. \tag{11}$$

Here $\alpha = 2\omega\kappa/c$ is the absorption coefficient. Since the position x of the leading edge of the coherent wavepacket is given by $x = x_\mathrm{o} + C_\mathrm{s}t$ with C_s the longitudinal acoustic sound

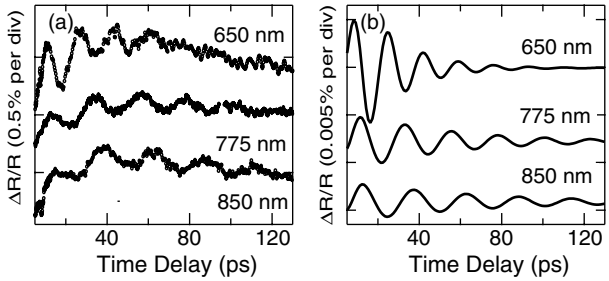

Figure 14. Experimental (a) and theoretical (b) coherent phonon differential reflectivity oscillations for probe wavelengths of 650, 775 and 850 nm. Note the change in period, the amplitude and the number of oscillations as the wavelength is changed and as predicted by theory.

velocity in the GaSb barrier, this allows us to determine the period of oscillation as

$$T = \frac{\lambda}{2C_s n(\lambda)} \tag{12}$$

where $\lambda = 2\pi\ c/\omega$ is the probe wavelength, and $n(\lambda)$ is the wavelength-dependent refractive index.

Note that the reflectivity oscillations are damped by a factor $e^{-\alpha x}$. This *does not occur* because the coherent acoustic phonons are damped and decay. It occurs, instead, because of the absorption of the probe pulse. One can probe only near the interface and the effect of the coherent phonon is diminished as it propagates away from the surface.

Using this simple model, we can compare the oscillations in the experimental differential reflectivity curves with our calculated differential reflectivity oscillations [66]. In figure 14 the computed coherent phonon differential reflectivity oscillations are shown as a function of time delay for probe wavelengths of 650, 775 and 850 nm, corresponding to photon energies of 1.9, 1.6, and 1.46 eV respectively. The theoretical differential reflectivity curves in figure 14(b) agree well with the experimentally measured differential reflectivity seen in figure 14(a) after subtraction of the transient background signal. As we go from 650 to 850 nm, the differential reflectivity oscillation period becomes longer, as predicted by equation (12). In addition, we see that the damping of the oscillation is in agreement with equation (11). As one goes to lower wavelengths (and thus higher laser energies), one probes at greater energies above the band gap where the absorption coefficient α increases and the oscillations die out more quickly.

In figure 15 we have plotted: (a) the index of refraction of GaSb and (b) the corresponding oscillation period as a function of wavelength derived from equation (12). In (c) we show the experimentally measured coherent phonon differential reflectivity oscillation periods as a function of probe wavelength as open circles. The solid line shows the oscillation period versus probe wavelength estimated using equation (12). The excellent agreement between theory and experiment is compelling evidence that the reflectivity oscillations seen in the experiments are indeed induced by propagating coherent acoustic phonons in the GaSb barrier.

In going from a probe wavelength of 650–850 nm in figure 14, we note that the initial amplitude of the differential reflectivity oscillation decreases with increasing probe wavelength. At the same time these oscillations become more weakly damped. The reason for the reduction in amplitude of the oscillations can be found in figure 16 where we plot $d\varepsilon/d\varepsilon_{zz}$ the derivative of the dielectric function with respect to strain ε_{zz} as a function of probe wavelength. The change in the dielectric function and hence the complex index of refraction $\delta\tilde{n}$ can be shown [66] to depend upon $d\varepsilon/d\varepsilon_{zz}$. As the probe wavelength increases (and the photon energy decreases), the strength of the perturbation of the dielectric function due to the propagating coherent

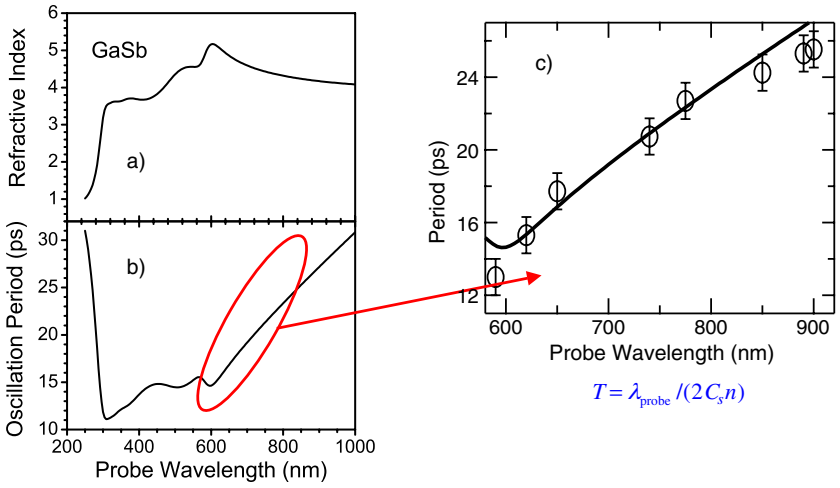

Figure 15. Index of refraction of GaSb (a) and the corresponding oscillation period (b) as a function of wavelength. (c) The coherent phonon differential reflectivity oscillation period versus probe wavelength in the region of interest. The experimental data are shown as open circles, and the solid line shows the oscillation period estimated from the simple theory $T = \lambda_{probe}/(2C_s n)$, demonstrating the agreement between experiment and theory.

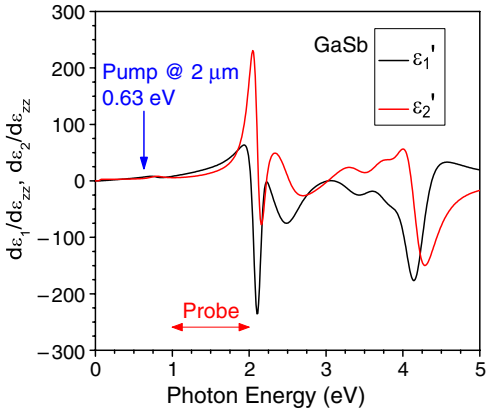

Figure 16. Derivative of the complex GaSb dielectric function with respect to strain as a function of the probe photon energy. The solid line is the real part and the dashed line is the imaginary part. Probing near 2 eV is enhanced due to the large value of the derivative.

phonon strain decreases. This accounts for the observed reduction in the initial amplitude of the differential reflectivity oscillations as we go to higher wavelengths. The increased damping of the differential reflectivity oscillations with decreasing probe wavelength is simply due to the fact that the absorption coefficient in GaSb is rapidly decreasing with wavelength in this wavelength range, as we have previously discussed.

4.2.3. Other carrier effects. In addition to modelling the oscillations in the differential reflectivity, we also worried about the fast time dynamics originating from the photo-excited carriers that gives rise to a time-dependent background signal. There are three main contributions to this transient background signal: (1) the enhanced Drude absorption resulting from the photo-induced increase in free carriers, (2) the relaxation dynamics associated with the decay of the highly nonequilibrium photo-excited carrier distribution and (3) the trapping

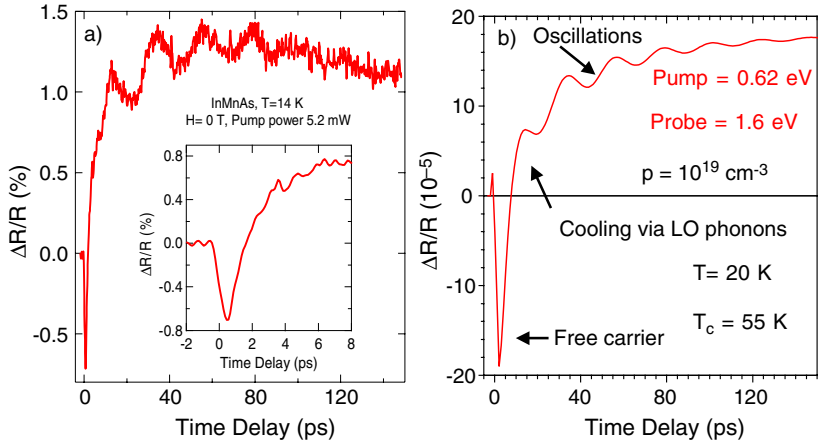

Figure 17. Experimental (a) and theoretical (b) differential reflectivity including the background effects of the carriers as well as the coherent phonon oscillations. The effects of induced free carrier absorption and cooling with LO phonons are included.

and subsequent non-radiative recombination of photo-excited carriers due to the high density of defects in the InMnAs layer.

To take into account this background signal, we first calculated the detailed electronic structure in the InMnAs layer based on a multiband $\vec{k} \cdot \vec{P}$ theory taking into account the Mn impurities [67, 68]. We then used a Boltzmann equation formalism to account for the photo-excited carrier dynamics [69–71]. In our dynamics, we include bandgap renormalization, carrier–phonon scattering, and carrier-trapping/recombination through the Shockley–Read mechanism. Finally, to more accurately determine the optical properties, we solved Maxwell's equations in the heterostructure using a transfer matrix technique to allow for a spatially and temporally varying dielectric function. Details of these calculations are given in [66].

Our theoretical results are compared with experiment in figure 17. We plot (a) the experimental and (b) the theoretical differential reflectivity spectra for a pump laser energy of 0.62 eV and a probe energy of 1.6 eV. In both cases, there is an initial sharp drop in the differential reflectivity which we attribute to free carrier Drude absorption by the hot carriers created by the pump.

The photo-generated hot carriers relax back to quasi-equilibrium distributions at their respective band edges through emission of confined LO phonons. The relaxation of photo-generated carriers by LO phonons alters the quantum well dielectric function through changes in the time-dependent distribution functions. This carrier cooling by LO phonon emission results in the subsequent rise in the differential reflectivity traces seen in figure 17.

In addition to carrier cooling by LO phonon emission, electron–hole pairs recombine through trapping at mid-gap defects with $\tau_0 \approx 200$ ps. This gives rise to the slow decay in the differential reflectivity at long times seen in figure 17. At short times, electron–hole pair recombination is enhanced since the Shockley–Read recombination time, $\tau(t)$, is a monotonically decreasing function of the photo-generated electron–hole pair density.

For delay times of less than 20 ps, there is some disagreement between theory and experiment. For delay times greater than 20 ps, however, the theory reproduces the experimental results surprisingly well. In particular, the period and amplitude of the reflectivity oscillations in relation to the height of the plateau as well as the decay of the reflectivity oscillations with delay time are in good agreement with experiment.

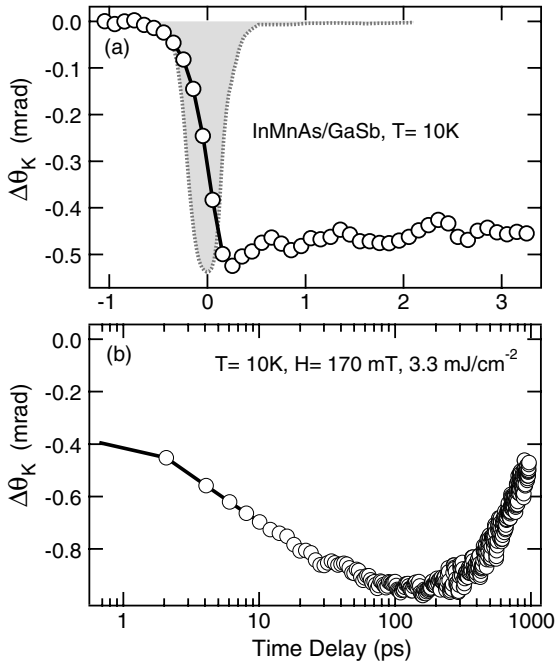

Figure 18. (a) The first 3 ps of demagnetization dynamics in InMnAs/GaSb. Also shown is the cross-correlation between the pump and probe pulses. (b) Demagnetization dynamics covering the entire time range of the experiment (up to ∼1 ns). There is a slow demagnetization process, which follows the fast component shown in (a) and completes only after ∼100 ps [43].

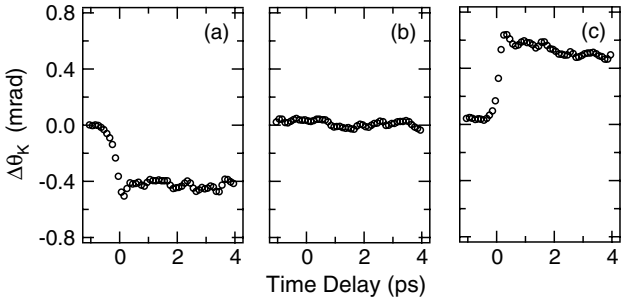

Figure 19. Initial decay of photo-induced Kerr rotation angle for three magnetic fields: (a) 7 mT, (b) 0 mT and (c) −7 mT. The sign of the MOKE angle change depends on the direction of the applied magnetic field in a symmetric manner [43].

4.3. Spin dynamics

4.3.1. Ultrafast demagnetization and quenching of ferromagnetism in InMnAs. Typical data showing the general temporal profile of the photo-induced Kerr angle change, $\Delta\theta_K$, are shown in figure 18, for the first 3 ps (in (a)) and the entire time range (in (b)). The sign of $\Delta\theta_K/\theta_K$ is always negative, indicating transient *demagnetization*. Distinct temporal regimes can be identified: an initial (<1 ps) rapid reduction in magnetization is followed by a slow and gradual decrease (up to ∼100 ps), a plateau region (up to ∼500 ps), and, finally, an increase (i.e., recovery) toward the equilibrium value. Also shown in figure 18(a) is the cross-correlation trace between the pump and probe pulses, showing that the initial ultrafast demagnetization is occurring even more quickly than our time resolution (∼220 fs).

Results showing the photo-induced Kerr angle for ferromagnetic InMnAs in the first 4 ps and under three different magnetic field conditions, +7 mT, 0 mT, and −7 mT, are presented in figures 19(a), (b) and (c). The sign of $\Delta\theta_K$ changes when the direction of the field is reversed, as expected for demagnetization. This claim is further substantiated by the fact that the photo-induced MOKE signal and the transient signals completely disappear at zero field. In the

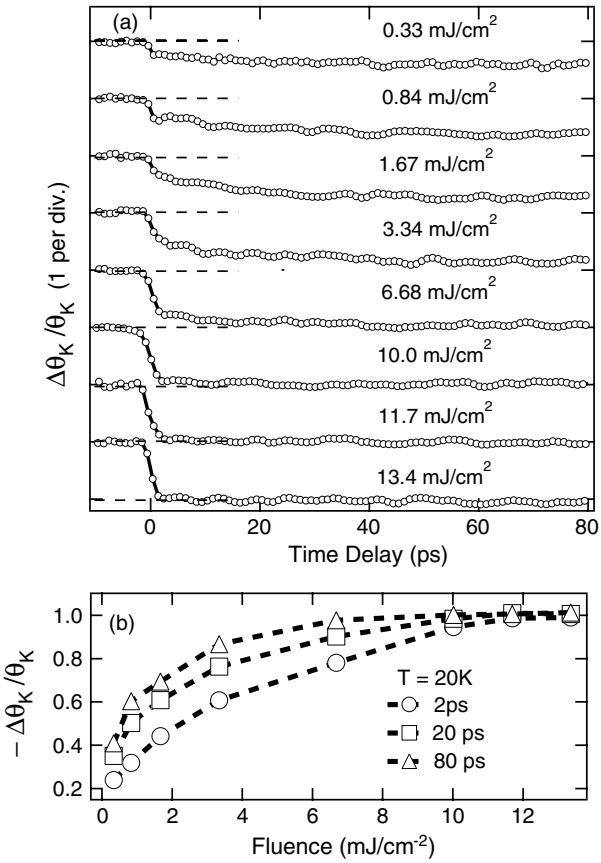

Figure 20. Normalized photo-induced MOKE angle change (a) versus time for different pump fluences and (b) versus pump fluence for different time delays. At high fluences, the signal saturates to ∼1, suggesting a complete quenching of ferromagnetic order [43].

following discussion, we define the photo-induced Kerr rotation as

$$\Delta\theta_{\mathrm{K}} = \tfrac{1}{2}[\Delta\theta_{\mathrm{K}}(-M) - \Delta\theta_{\mathrm{K}}(+M)] \tag{13}$$

in order to eliminate any possible nonmagnetic contributions to the transient MOKE signal, e.g., pump-induced optical anisotropy and two-photon coherence.

Photo-induced Kerr rotation dynamics, normalized by the MOKE angle before the arrival of the pump, is plotted for different pump fluences in figure 20(a). At low pump fluences, the fast (<1 ps) and slow (∼100 ps) demagnetization components coexist. However, as the fluence increases, the fast component progressively becomes more dominant. Around ∼10 mJ cm^{-2}, there is no slow demagnetization process—a sharp initial drop is followed by a completely flat region. This 'step-function' like response remains stable both in shape and magnitude against further increases in pump fluence to 13.4 mJ cm^{-2}, i.e., the demagnetization saturates. The saturation value is 1, implying that the change in magnetization is 100% (see also figure 20(b)). These results suggest that a *complete quenching* of the ferromagnetic order occurs on a timescale of several hundred femtoseconds.

To substantiate the above claims, we also perform further measurements and make the following arguments.

(i) At high pump fluence, a ferromagnetic to paramagnetic phase transition, seen as a saturation of $\Delta\theta_{\mathrm{K}}$ to unity, as a function of pump fluence was observed on the sub-picosecond timescale. At this extreme condition, there is no doubt that ultrafast

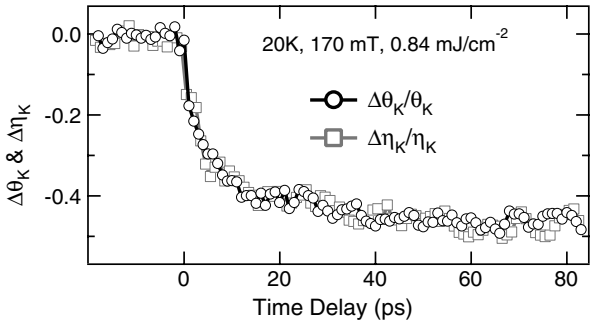

Figure 21. Temporal profiles of normalized Kerr/ellipticity angle.

demagnetization occurs over several hundred femtoseconds. Therefore, at intermediate pump power, it is natural to assign the origin of the sub-picosecond component, coexisting with the slow component of 100 ps, to demagnetization.

(ii) We also performed temperature-dependent measurements, and the results are shown in figure 22(a). Here, a strong temperature dependence of both the fast and slow components is seen. $\Delta\theta_K$ decreases drastically as the temperature approaches the critical temperature T_c (∼60 K), and $\Delta\theta_K$ is *absent above* T_c. These facts further suggest that the transient Kerr rotation here measures the magnetization change of the ferromagnetic state (figure 22(b)).

(iii) In order to further eliminate the possibility that the induced MOKE changes are due to purely optical effects, we also monitored both MOKE and reflection MCD at the same time. The exact coincidence between MOKE and MCD is shown in figure 25(c). In addition, their size is much larger than that of the reflectivity. In the current measurements, the differential reflectivity is of the order of 1% at the highest pump fluence, while normalized Kerr/MCD rotation can be as high as 100%. Thus

$$\frac{\Delta\theta_k(t)}{(\theta_K)_0} = \frac{\Delta\eta_k(t)}{(\eta_k)_0} \gg \frac{\Delta R(t)}{R_0}. \tag{14}$$

Figure 21 shows one example where the normalized Kerr and MCD rotation have similar temporal profiles and much larger size in comparison with the differential reflectivity, ensuring that we are probing magnetic properties (see, e.g., [18]).

Finally, let us turn our attention to long-term recovery dynamics of the MOKE signal as shown in figure 23. At a high pump fluence (∼10.0 mJ cm^{-2}) where $\Delta\theta$ approaches unity, the photo-induced MOKE signal stays almost unchanged up to 900 ps, showing a much slower recovery compared to that at a relatively low pump fluence, e.g., ∼3.34 mJ cm^{-2}. This observation may be understood as follows. At relatively low pump fluence where the magnetic order is not completely destroyed, the recovery of the ground state involves expanding the ferromagnetic domains. However, recovery from a completely quenched state, as in the case of a high pump fluence, requires the local nucleation of ferromagnetism first, followed by similar domain expansion processes, manifesting itself as a slower recovery of the ground state.

4.3.2. Ultrafast magnetization dynamics in ferromagnetic GaMnAs. For LT-MBE grown ferromagnetic GaMnAs, the existence of a characteristic 'band tailing' absorption due to Mn impurity and As_{Ga} antisite defect bands, located around 100 and 500 meV above the valence band, respectively, has been well established (inset, figure 24). In particular, a femtosecond mid-infrared excitation tuned to As_{Ga} antisite absorption centred at ∼2 μm

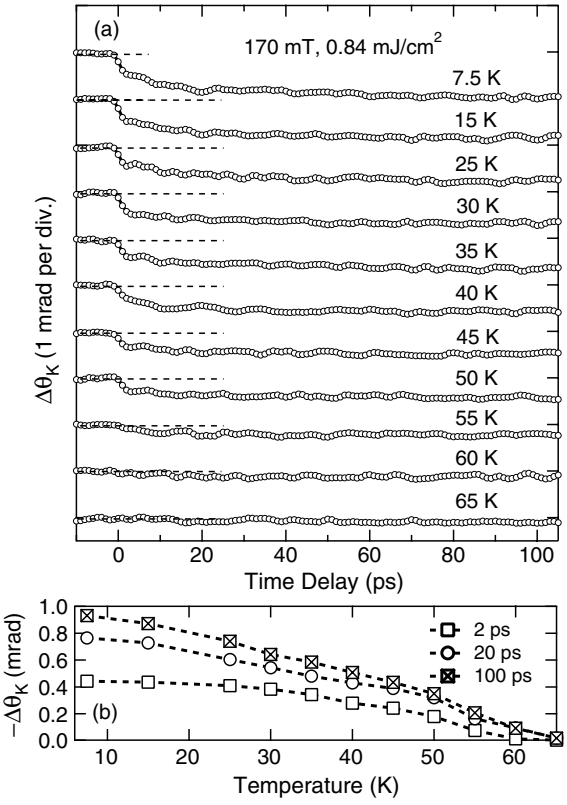

Figure 22. Photo-induced MOKE angle change (a) versus time for different temperatures and (b) versus temperature for different time delays. The photo-induced change is absent above the Curie temperature (∼60 K).

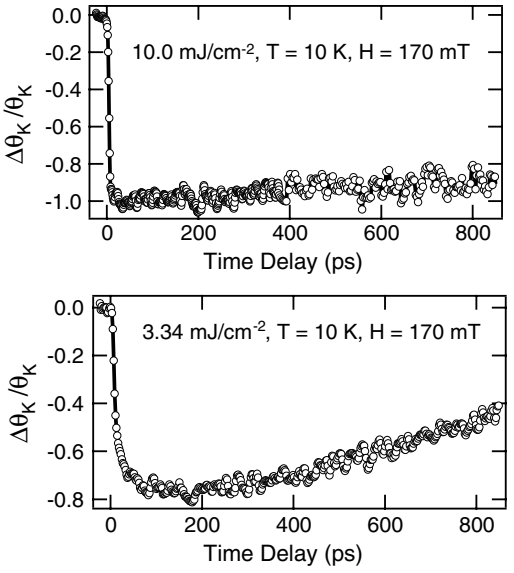

Figure 23. Time evolution of photo-induced Kerr rotation for two different pump fluences. At high pump fluence (∼10.0 mJ cm^{-2}), a long recovery time of ferromagnetic ground state is observed, in comparison to the relatively fast recovery in low pump fluence condition (∼3.34 mJ cm^{-2}).

generates *delocalized, transient holes* and *localized, trapped electrons*, which allows us to study the correlation between hole dynamics and induced magnetization dynamics on femtosecond timescales.

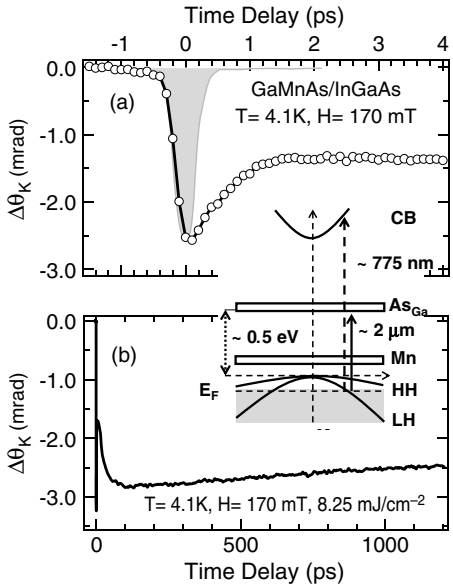

Figure 24. (a) The first 4 ps of $\Delta\theta_K$ dynamics in GaMnAs/InGaAs. The shaded area is the pump–probe cross-correlation. (b) Temporal behaviour of $\Delta\theta_K$ converting the entire time range of the experiment (up to 1.2 ns). The inset shows a schematic band diagram of p-GaMnAs and selective pump–probe method. MIR pump pulses at 2 μm (solid line) only generate *delocalized, transient carriers (holes)* in the valence band via intragap excitations from the top of Fermi level to As_{Ga} antisite defect band, centred ∼0.5 eV above valence band. The change in MOKE rotation is probed by a reflected, time-delayed synchronized NIR pulse at 775 nm (dashed line), corresponding to the interband transitions close to the fundamental band gap.

Typical polar MOKE dynamics in ferromagnetic GaMnAs is shown in figure 24. The initial change in the MOKE signal is negative, followed by a quick recovery of the negative signal with time constants of ∼800 fs shown in (a) and a slow decrease ∼100 ps shown in (b). Finally, the signal shows a very slow recovery of ∼2 ns.

The sign of $\Delta\theta_K/\theta_K$ changes when the direction of the field is reversed, consistent with ultrafast demagnetization. Temporal evolution and the magnitude of $\Delta R/R$ also show a magnetic field dependence, clearly indicating transverse MOKE effects. We can isolate transverse MOKE components ΔT-MOKE, and magnetization-dependent $\Delta R/R$, by subtracting two $\Delta R/R$ traces taken with magnetic fields of opposite sign. Transverse MOKE dynamics shows a similar femtosecond demagnetization and slow demagnetization component of the order of 100 ps as in polar MOKE $\Delta\theta_K$ dynamics. It is also important to notice that there is an initial 'overshoot' component existing only in the polar MOKE profile.

4.3.3. Ultrafast softening in ferromagnetic InMnAs. In this section we will discuss a different transient magnetic phenomenon, which appears under relatively low pump fluence in comparison to those used in ultrafast demagnetization experiments. Figure 26 presents the detailed time evolution of ferromagnetic hysteresis loops in InMnAs at 20 K, demonstrating femtosecond photo-induced softening. Ferromagnetic loops at fixed time delays are plotted in figures 26(a)–(h). The data at negative time delays (figures 26(a), (b)) show hysteresis loops with a finite coercivity. However, at a time delay of 450 fs (figures 26(c), (d)), the hysteresis loops are totally suppressed in the horizontal direction, i.e., the coercivity is almost zero. Note

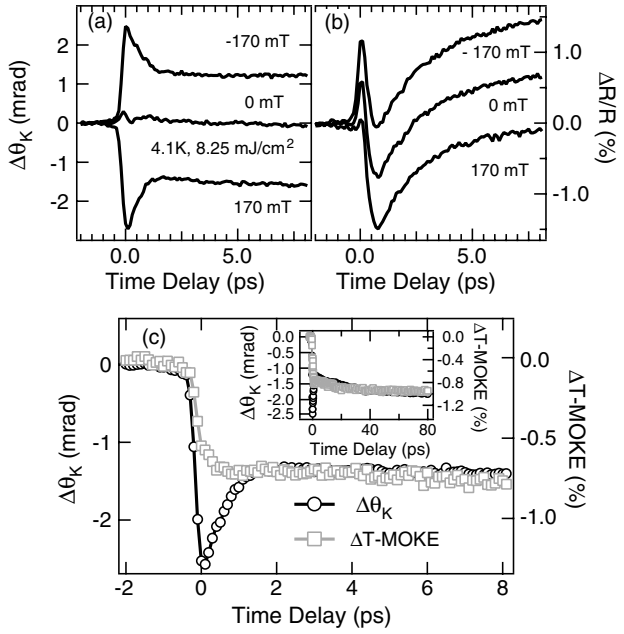

Figure 25. Magnetic field dependence of polar MOKE $\Delta\theta_K$ dynamics (a) and differential reflectivity $\Delta R/R$ (b). (c) Transverse MOKE ΔT-MOKE dynamics, extracted by subtracting between two $\Delta R/R$ traces under opposite signs of the magnetic field is plotted together with $\Delta\theta_K$ for the first 8 ps and up to 80 ps (inset), showing the same femtosecond demagnetization and slow demagnetization component of the order of 100 ps, i.e., no time lag between $\Delta\theta_K$ and ΔT-MOKE except an initial 'overshoot' component in $\Delta\theta_K$.

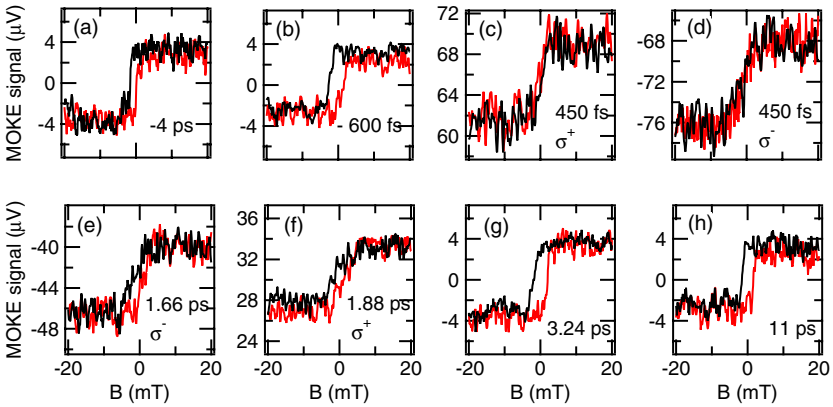

Figure 26. Ultrafast photo-induced softening in InMnAs. (a)–(h) MOKE signals versus field at different time delays under pumping with circularly polarized light at 2 μm radiation. (a) 4 ps; (b) 600 fs; (c) 450 fs, pump was circularly polarized (σ^+); (d) 450 fs, σ^-; (e) 1.66 ps, σ^-; (f) 1.88 ps, σ^+; (g) 3.24 ps; (h) 11 ps. A ferromagnetic hysteresis loop with finite coercivity is clearly seen in (a) and (b). In (c) and (d), the loop is nearly destroyed in the horizontal direction, i.e., the coercivity is almost zero.

that the ferromagnetic hysteresis loops change direction under different pumping conditions, i.e., right- and left-circularly polarized states. The magnetic hysteresis loops continue to evolve

and the softening lasts a few picoseconds (figures 26(e) and (f)). After this short period of time, loops with the original H_c are recovered (figures 26(g) and (h)). We should also notice that almost no change is observed in the vertical height of the loop within the sensitivity of our setup (the sensitivity of this setup, based on a lock-in detection and a Nirvana balanced detector, limited itself to seeing any horizontal shrinkage discussed in the previous section).

We believe that carrier-enhanced exchange coupling between Mn ions is at the core of the observed ultrafast photo-induced softening. The phenomenon is essentially the same as what has been observed in the CW work on the same systems [72] except for the very different timescales.

4.3.4. Discussion and theory of ultrafast demagnetization in (III,Mn)V compounds. In this section we will discuss the ultrafast (sub-picosecond) photo-induced dynamics of the coupled systems of holes and Mn spins. The experimentally observed long-time dynamics (100 ps timescale) fits the traditional framework of spin–lattice relaxation and subsequent cooling due to heat diffusion out of the laser spot. It is the fast drop of the Kerr signal that requires an explanation.

In diluted magnetic semiconductors the interaction between the carriers (electrons and holes) and the localized Mn spins is governed by the sp–d Hamiltonian of the Kondo-like form $H_{\mathrm{sp-d}} \propto \beta \mathbf{Ss}$, where $\mathbf{S}$ and $\mathbf{s}$ represent, respectively, the Mn and the carrier spin, and the typical value of exchange constant β is 50 meV nm^3 for holes [73]. The (III,Mn)V ferromagnetic semiconductors are heavily p-doped, with hole concentrations of the order of 10^{20} cm^{-3}, and these holes mediate the Mn–Mn spin interaction leading to ferromagnetism [10]. The sp–d Hamiltonian is

$$H_{\mathrm{sp-d}} \propto \beta\left(S_z s_z + \tfrac{1}{2} S_+ s_- + \tfrac{1}{2} S_- s_+\right), \tag{15}$$

where $S_\pm$ are the usual spin ladder operators. The first term proportional to $S_z s_z$ is treated in the mean-field approximation, replacing the operator S_z by its mean value. This leads to the splitting of the valence bands, and the requirement of self-consistency of effective fields acting on Mn and hole spins allows derivation of the critical temperature [45, 74]. The spin splitting of the conduction and valence bands causes the absorption coefficients for two the circular polarizations of light to differ, leading to the magneto-optical activity.

Scattering between the carriers and Mn spins can lead to spin-flips (the off-diagonal terms in equation (15)). In equilibrium, the net number of spin-flips is zero (by definition), but when the carrier population is excited (brought out of equilibrium with the Mn spin system), a net flow of energy and angular momentum can occur between these subsystems. This excitation is created by the laser pump, which creates new photo-excited carriers (electrons and holes). The spin scattering for holes is more efficient: the larger density of states and stronger exchange interaction increase the scattering probability. Consequently, we will concentrate exclusively on nonequilibrium holes, as the theory predicts that electrons do not influence the magnetization quenching process. This is supported by the experimental results on GaMnAs, where no conduction band electrons are excited, and the demagnetization is similar to the case in InMnAs.

Let us consider an excited population of holes. After the thermalization time ($\sim$100 fs) the holes are described by a Fermi distribution with a temperature higher than the lattice temperature. In the following we will describe the hole distribution in terms of the hole temperature T_h even for the initial stage of the dynamics, which is a rough approximation. The elevated T_h causes a blurring of the Fermi surface, which strongly increases the number of states available for spin-flip scattering. This allows for the flow of energy and angular momentum between the hot holes and localized spins. The demagnetization is caused by the transfer

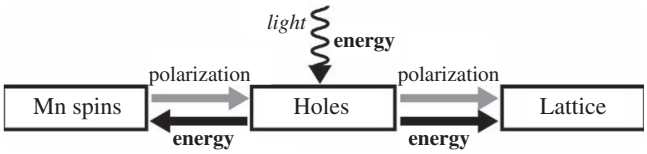

Figure 27. A schematic depiction of the inverse Overhauser effect. The holes are out of equilibrium with the localized spins and the lattice.

of polarization (spin/angular momentum) from Mn spins to holes, which is sustained by the efficient spin relaxation of holes. Without the latter process, which comes from interactions not included in the sp–d Hamiltonian (hole–hole, hole–disorder and hole–phonon scattering), the Mn depolarization would cease very quickly, as the dynamical polarization of the hole population effectively blocks the spin-flip scattering. It should be noted that each hole has to take part in multiple spin-flip scatterings, in order to account for the sizable demagnetization visible in experiments. This follows from the ratio of the number of Mn spins to holes, which is larger than one due to compensation, and the $\frac{5}{2}$ value of the Mn spin compared to one-half for the hole. The whole process can be envisioned as the reverse of the Overhauser effect [75]; the excited carriers become dynamically polarized at the expense of the localized spins, and the dissipation of magnetization occurs through spin relaxation in the carrier system (see figure 27).

The same spin-flip scattering mechanism has been used to describe the CW heating of Mn spins by a photo-excited two-dimensional electron gas in paramagnetic CdMnTe [76], but the basic idea is much older. The model of magnetization relaxation through spin-flips with carriers with subsequent spin relaxation by spin–orbit interaction can be traced back as far as the 1950s [77], and this approach has recently reappeared in the ferromagnetic semiconductor literature [78, 79].

We describe the dynamics of Mn spins by a rate equation for the diagonal elements of the localized spin density matrix [80]

$$\frac{\mathrm{d}N_m}{\mathrm{d}t} = \sum_{m'} (W_{mm'} N_{m'} - W_{m'm} N_m) \tag{16}$$

where $m = -\frac{5}{2} \ldots \frac{5}{2}$ and N_m is the population of the mth level of the Mn spin. $W_{mm'}$ is the probability of a spin-flip of the Mn spin from $S_z = m'$ to m, and in the one-band model it is given by

$$W_{m,m'} = \frac{2\pi}{\hbar} \frac{\beta^2}{4} \sum_{\mathrm{s},s'} \int \frac{\mathrm{d}^3 k}{(2\pi)^3} \int \frac{\mathrm{d}^3 q}{(2\pi)^3} f_{s'}(\mathbf{k})(1 - f_{\mathrm{s}}(\mathbf{q})) \times \delta(\epsilon_{\mathrm{s}}(\mathbf{q}) - \epsilon_{s'}(\mathbf{k}) \pm \delta) |\langle ms|\hat{S}_{\pm}\hat{s}_{\mp}|m's'\rangle|^2, \tag{17}$$

where $\epsilon_{\mathrm{s}}(\mathbf{k})$ is the energy of the hole with spin s and δ is the splitting of the localized spin (with Mn spin energy E_m, we have $\delta = E_{m+1} - E_m$), which is of the order of 1 meV. The mean-field spin splitting of holes $\Delta = \epsilon_+(\mathbf{k}) - \epsilon_-(\mathbf{k})$ is proportional to the average Mn spin $M = \sum_m m N_m$, and for the saturation magnetization in a typical (III,Mn)V material we have $\Delta \approx 100$ meV. The occupation functions $f_{\mathrm{s}}(\mathbf{k})$ are thermal, with a high effective temperature T_{h}, and with possibly different quasi-Fermi levels for the two spin orientations. The latter feature allows us to capture the dynamic polarization of holes. Finally, the dynamics of the average hole spin s (proportional to the difference in the number of holes with spins up and down) is described by [81]

$$\frac{\mathrm{d}s}{\mathrm{d}t} = -\gamma \frac{\mathrm{d}M}{\mathrm{d}t} - \frac{1}{\tau_{\mathrm{s}}}(s - s_{\mathrm{eq}}(M, T_{\mathrm{h}})), \tag{18}$$

where γ is the ratio of Mn to hole density, s_{eq} is the instantaneous equilibrium value of the average hole spin, and τ_{s} is the spin relaxation time. Strong spin–orbit interaction in the valence

band leads to close correlation between the momentum scattering and spin relaxation times. The presence of strong disorder in the ferromagnetic semiconductors results in momentum scattering times of the order of 10 fs [82] (corresponding to the quasiparticle broadening of about 100 meV). Furthermore, in the excited hole population the h–h and phonon scattering is enhanced compared to the equilibrium case, allowing us to assume $\tau_s < 100$ fs. This is confirmed by the experimental results in GaMnAs, where no pump–polarization-dependent response is seen, showing that the photo-generated spin-polarized holes lose their orientation on a timescale much below the pulse temporal width.

In the calculations we use $T_h = 1000$ K, which gives an energy spread of the holes comparable to the exchange splitting of the band. The calculated transfer of heat from hot holes to the localized spins does not significantly change this temperature, and the cooling of the holes is caused by phonon emission, which is expected to be very efficient for highly excited holes [83]. The drop of T_h within a picosecond puts a stop to the 'inverse Overhauser' process. Consequently, we solve our equations with constant T_h for a short time. Using $\tau_s = 10$ fs, $p = 4 \times 10^{20}$ cm^{-3}, band mass $m_h = 0.5m_0$, and typical values of β we obtain a drop in magnetization of 10% within 200 fs. This result shows that the ultrafast demagnetization in these materials is possible, and qualitative agreement with experiments supports the underlying physical picture. In order to refine the model presented above and verify its parameters, more theoretical work on strong photo-excitation of disordered III–V magnetic semiconductors and spin relaxation of hot holes is needed.

5. Summary

The topics studied in this review article demonstrate the strength of magneto-optical spectroscopy in investigating spin-related phenomena in condensed matter. Magneto-optical spectroscopy combined with femtosecond laser pulses, provides direct time-domain information about magnetic properties of excited states with high temporal resolution and fine control. Until now, (III,Mn)V ferromagnets have been studied quite extensively using static optical or transport methods; time-domain spectroscopy has rarely been attempted and has not proven to be a powerful probe. Newly developed two-colour methods of MOKE and MCD spectroscopy have been described and experimental results on charge dynamics, phonon dynamics, and spin dynamics, respectively, have been presented.

Regarding charge dynamics, the dynamics of photo-generated carriers in InMnAs, InGaMnAs, and GaMnAs were discussed. Results of time-resolved two-colour transient reflectivity measurements with a mid-infrared pump and a single-colour near-infrared probe were presented. Very short carrier lifetimes ($\sim$2 ps) and multilevel charge decay dynamics are observed. The salient features of carrier relaxation contain some unique properties of (III,Mn)V semiconductors, such as the existence of large-density mid-bandgap states and heavy Mn p-doping.

The transient reflectivity technique also provides direct information about phonon dynamics. An oscillatory component in the transient reflectivity, whose period, amplitude and damping are strong functions of the probe laser energy, is associated with propagating coherent acoustic phonon (CAP) wavepackets. The CAP observed for the first time in (III,Mn)Vs is similar to what has been seen in GaN/InGaN epilayers. However, the generation mechanism of CAP is via a deformation potential coupling mechanism in (III,Mn)Vs, instead of screening of piezoelectric fields in GaN/InGaN epilayers.

Next, the spin relaxation of photo-injected carriers and demagnetization dynamics were discussed. The coexistence of fast ($<$1 ps) and slow ($\sim$100 ps) demagnetization processes, previously unobserved in laser excited ferromagnetic metals and insulators, is observed for both ferromagnetic InMnAs and GaMnAs. In particular, in an InMnAs/GaSb single heterostructure,

a femtosecond quenching of ferromagnetic order is observed. We attribute the fast dynamics to spin heating through sp–d exchange interaction between photo-carriers and Mn ions while the ∼100 ps component is interpreted as spin–lattice relaxation. In addition, ultrafast photo-induced softening in ferromagnetic InMnAs is shown and a qualitative picture is given.

Acknowledgments

This work was supported by DARPA (MDA972-00-1-0034), NSF (DMR-0134058, DMR-0325474, DMR-0325599, INT-0221704, and OISE-0530220), ONR (N000140410657), MEXT (No.14076210), and DOE (DE-FG02-02ER45984). We thank Akira Oiwa for technical assistance.

References

[1] Baibich M N, Broto J M, Fert A, Van Dau N, Petroff, Eitenne F, Creuzet P, Friederich G and Chazelas A 1988 *Phys. Rev. Lett.* **61** 2472
[2] Pearton S J, Norton D P, Frazier R, Han S Y, Abernathy C R and Zavada J M 2005 *IEE Proc.* **152** 312 (Review article)
[3] Munekata H, Ohno H, Von Molnar S, Segmüller A, Chang L L and Esaki L 1989 *Phys. Rev. Lett.* **63** 1849
[4] Ohno H, Munekata H, Penney T, Von Molnar S and Chang L L 1992 *Phys. Rev. Lett.* **68** 2664
[5] Munekata H, Zaslavsky A, Fumagalli P and Gambino R J 1993 *Appl. Phys. Lett.* **63** 2929
[6] Ohno H, Shen A, Matsukura F, Oiwa A, Endo A, Katsumoto S and Iye Y 1996 *Appl. Phys. Lett.* **69** 363
[7] SÏupiński T, Oiwa A, Yanagi S and Munekata H 2002 *J. Cryst. Growth* **1326** 237
[8] Matsumoto Y, Murakami M, Shono T, Hasegawa T, Fukumura T, Kawasaki M, Ahmet P, Chikyow T, Koshihara S and Koinuma H 2001 *Science* **291** 854
[9] Ueda K, Tabata H and Kawai T 2001 *Appl. Phys. Lett.* **79** 988
[10] Dietl T, Ohno H, Matsukura F, Cibert J and Ferrand D 2000 *Science* **287** 1019
[11] Nazmul M, Kobayashi S, Sugahara S and Tanaka M 2004 *Physica* E **21** 937
[12] Koshihara S, Oiwa A, Hirasawa M, Katsumoto S, Iye Y, Urano C, Takagi H and Munekata H 1997 *Phys. Rev. Lett.* **78** 4617
[13] Ohno H, Chiba D, Matsukura F, Omiya T, Abe E, Dietl T, Ohno Y and Ohtani K 2000 *Nature* **408** 944
[14] Awschalom D D and Samarth N 2002 *Semiconductor Spintronics and Quantum Computation* ed D D Awschalom, D Loss and N Samarth (Berlin: Springer) pp 147–92
[15] Zhang G, Hübner W, Beaurepaire E and Bigot J-Y 2002 *Spin Dynamics in Confined Magnetic Structures I* ed B Hillebrands and K Ounadjela (Berlin: Springer) pp 245–88
[16] Beaurepaire E, Merle J-C, Daunois A and Bigot J-Y 1996 *Phys. Rev. Lett.* **76** 4520
[17] Beaurepaire E, Merle J-C, Daunois A and Bigot J-Y 1998 *Phys. Rev.* B **58** 12134
[18] Koopmans B, van Kampen M, Kohlhepp J T and de Jonge W J M 2000 *Phys. Rev. Lett.* **85** 844
[19] Guidoni L, Beaurepaire E and Bigot J Y 2002 *Phys. Rev. Lett.* **89** 017401
[20] Zhang G P and Hübner W 2000 *Phys. Rev. Lett.* **85** 3025
[21] Kimel A V, Astakhov G V, Schott G M, Kirilyuk A, Yakovlev D R, Karczewski G, Ossau W, Schmidt G, Molenkamp L W and Rasing Th 2004 *Phys. Rev. Lett.* **92** 237203
[22] Gómez-Abal R, Ney O, Satitkovitchai K and Hübner W 2004 *Phys. Rev. Lett.* **92** 227402
[23] Kimel A V, Kirilyuk A, Usachev P A, Pisarev R V, Balbashov A M and Rasing Th 2005 *Nature* **435** 655
[24] Oiwa A, Mitsumori Y, Moriya R, SÏupiński T and Munekata H 2002 *Phys. Rev. Lett.* **88** 137202
[25] Kimel A V, Kirilyuk A, Tsvetkov A, Pisarev R V and Rasing T 2004 *Nature* **429** 850
[26] Kojima E, Shimano R, Hashimoto Y, Katsumoto S, Iye Y and Kuwata-Gonokami M 2003 *Phys. Rev.* B **68** 193203
[27] Kojima E, Heroux J B, Shimano R, Hashimoto Y, Katsumoto S, Iye Y and Kuwata-Gonokami M 2004 *Preprint* cond-mat/0408030
[28] Mitsumori Y, Oiwa A, SÏupiński T, Maruki H, Kashimura Y, Minami F and Munekata H 2004 *Phys. Rev.* B **69** 033203
[29] Crooker S A, Baumberg J J, Flack F, Samarth N and Awschalom D D 1996 *Phys. Rev. Lett.* **77** 2814
[30] Krenn H, Kaltenegger K, Dietl T, Spałek J and Bauer G 1989 *Phys. Rev.* B **39** 10918
[31] Linder N and Sham L J 1998 *Physica* E **2** 412
[32] Chovan J, Kavousanaki E G and Perakis I E 2006 *Phys. Rev. Lett.* **96** 057402
[33] Fernández-Rossier J, Núñez A S, Abolfath M and MacDonald A H 2003 *Preprint* cond-mat/0304492

[34] Fernández-Rossier J, Piermarocchi C, Chen P, MacDonald A H and Sham L J 2004 *Phys. Rev. Lett.* **93** 127201
[35] Kaneko M 2000 *Magnetooptics* ed S Sugano and N Kojima (Berlin: Springer) pp 271–315
[36] Vaterlaus A, Beutler T and Meier F 1991 *Phys. Rev. Lett.* **67** 3314
[37] Vaterlaus A, Beutler T, Guarisco D, Lutz M and Meier F 1992 *Phys. Rev.* B **46** 5280
[38] Strutz T, Witowski A M and Wyder P 1992 *Phys. Rev. Lett.* **68** 3912
[39] Hübner W and Bennemann K H 1996 *Phys. Rev.* B **53** 3422
[40] Groeneveld R H M, Sprik R and Lagendijk A 1995 *Phys. Rev.* B **51** 11433
[41] Koopmans B, Kicken H H J E, van Kampen M and de Jonge W J M 2005 *J. Magn. Magn. Mater.* **286** 271
[42] Koopmans B, Ruigrok J J M, Dalla Longa F and de Jonge W J M 2005 *Phys. Rev. Lett.* **95** 267207
[43] Wang J, Sun C, Kono J, Oiwa A, Munekata H, Cywiński Ł and Sham L J 2005 *Phys. Rev. Lett.* **95** 167401
[44] Žutić I, Fabian J and Das Sarma S 2004 *Rev. Mod. Phys.* **76** 323
[45] Dietl T, Ohno H and Matsukura F 2001 *Phys. Rev.* B **63** 195205
[46] Oppeneer P M and Liebsch A 2004 *J. Phys.: Condens. Matter* **16** 5519
[47] Vernes A and Weinberger P 2005 *Phys. Rev.* B **71** 165108
[48] Bigot J Y, Guidoni L, Beaurepaire E and Saeta P N 2004 *Phys. Rev. Lett.* **93** 077401
[49] Kampfrath T, Ulbrich R G, Leuenberger F, Münzenberg M, Sass B and Felsch W 2002 *Phys. Rev.* B **65** 104429
[50] Koopmans B, van Kampen M and de Jonge W J M 2003 *J. Phys.: Condens. Matter* **15** S723
[51] Hohlfeld J, Matthias E, Knorren R and Bennemann K H 1997 *Phys. Rev. Lett.* **78** 4861
[52] Scholl A, Baumgarten L, Jacquemin R and Eberhardt W 1997 *Phys. Rev. Lett.* **79** 5146
[53] Melnikov A V, Güdde J and Matthias E 2002 *Appl. Phys.* B **74** 735
[54] Wang J, Khodaparast G A, Kono J, Slupinski T, Oiwa A and Munekata H 2003 *J. Supercond.: Incorporating Novel Magn.* **16** 373
[55] Wang J, Khodaparast G A, Kono J, Slupinski T, Oiwa A and Munekata H 2003 *Physica* E **20** 412
[56] Pan R-P, Wei H D and Shen Y R 1989 *Phys. Rev.* B **39** 1229
[57] Conrad U, Güdde J, Jähnke V and Matthias E 2001 *Phys. Rev.* B **63** 144417
[58] Wang J, Kono J, Slupinski T, Oiwa A, Munekata H and Stanton C J 2004 *Superlatt. Microstruct.* **34** 563
[59] Wang J, Hashimoto Y, Kono J, Oiwa A, Munekata H, Sanders G D and Stanton C J 2005 *Phys. Rev.* B **72** 153311
[60] Yahng J S, Jho Y D, Yee K J, Oh E, Woo J C, Kim D S, Sanders G D and Stanton C J 2004 *Appl. Phys. Lett.* **84** 5234
[61] Liu R, Kim C S, Sanders G D, Stanton C J, Yahng J S, Jho Y D, Yee K J, Oh E and Kim D S 2005 *Phys. Rev.* B **72** 195335
[62] Chern G-W, Sun C-K, Sanders G D and Stanton C J 2004 *Topics in Applied Physics* vol 92, ed K-T Tsen (New York: Springer) pp 339–94
[63] Stanton C J, Sanders G D, Liu R, Chern G-W, Sun C-K, Yahng J S, Jho Y D, Sohn J Y, Oh E and Kim D S 2003 *Superlatt. Microstruct.* **34** 525
[64] Słupiński T, Oiwa A, Yanagi S and Munekata H 2002 *J. Cryst. Growth* **237–239** 1326
[65] Wang J, Khodaparast G A, Kono J, Oiwa A and Munekata H 2004 *J. Mod. Opt.* **51** 2771
[66] Sanders G D, Stanton C J, Wang J, Kono J, Oiwa A and Munekata H 2005 *Phys. Rev.* B **72** 245302
[67] Sanders G D, Sun Y, Kyrychenko F V, Stanton C J, Khodaparast G A, Kono J, Matsuda Y H, Miura N and Munekata H 2003 *Phys. Rev.* B **68** 165205
[68] Matsuda Y H, Khodaparast G A, Zudov M A, Kono J, Sun Y, Kyrychenko F V, Sanders G D, Stanton C J, Miura N, Ikeda S, Hashimoto Y, Katsumoto S and Munekata H 2004 *Phys. Rev.* B **70** 195211
[69] Sanders G D, Sun C-K, Fujimoto J G, Choi H K, Wang C A and Stanton C J 1994 *Phys. Rev.* B **50** 8539
[70] Sanders G D, Sun C-K, Golubovic B, Fujimoto J G and Stanton C J 1996 *Phys. Rev.* B **54** 8005
[71] Sanders G D and Stanton C J 1998 *Phys. Rev.* B **57** 9148
[72] Oiwa A, S̈lupiński T and Munekata H 2001 *Appl. Phys. Lett.* **78** 518
[73] Furdyna J K 1988 *J. Appl. Phys.* **64** R29
[74] Fernández-Rossier J and Sham L J 2001 *Phys. Rev.* B **64** 235323
[75] Abragam A 1983 *The Principles of Nuclear Magnetism* (Oxford: Oxford University Press)
[76] König B, Merkulov I A, Yakovlev D R, Ossau W, Ryabchenko S M, Kutrowski M, Wojtowicz T, Karczewski G and Kossut J 2000 *Phys. Rev.* B **61** 16870
[77] Mitchell A H 1957 *Phys. Rev.* **105** 1439
[78] Sinova J, Jungwirth T, Liu X, Furdyna J K, Atkinson W A and MacDonald A H 2004 *Phys. Rev.* B **69** 085209
[79] Tserkovnyak Y, Fiete G A and Halperin B I 2004 *Appl. Phys. Lett.* **84** 5234
[80] Blum K 1981 *Density Matrix Theory And Applications* (New York: Plenum)
[81] Langreth D C and Wilkins J W 1972 *Phys. Rev.* B **6** 3189
[82] Jungwirth T, Abolfath M, Sinova J, Kucera J and MacDonald A H 2002 *Appl. Phys. Lett.* **81** 4029
[83] Woerner M and Elsaesser T 1995 *Phys. Rev.* B **51** 1749